# Experimental investigation of early strain heterogeneities and localizations in polycrystalline $\alpha$ -Fe during monotonic loading

Adrien Berger, Jean-Francois Witz, Ahmed El Bartali, Tarik Sadat, Nathalie Limodin, Mirentxu Dubar, Denis Najjar

# Experimental investigation of early strain heterogeneities and localizations in polycrystalline $\alpha$-Fe during monotonic loading

A. Berger[a, b, *], J-F. Witz[a], A. El Bartali[a], T. Sadat[c], N. Limodin[a], M. Dubar[c], D. Najjar[a]

January 28, 2022

a. Univ. Lille, CNRS, Centrale Lille, UMR 9013 - LaMcube - Laboratoire de Mécanique, Multiphysique, Multiéchelle, F-59000 Lille, France
b. MG-VALDUNES - BP 12 - Rue Gustave Delory - 59125 Trith-Saint-Leger - France
c. UPHF, CNRS, UMR 8201 - LAMIH - Laboratoire d'Automatique de Mécanique et d'Informatique Industrielles et Humaines, F-59313, Valenciennes, France
* Corresponding author. E-mail address: adrien.berger@centralelille.fr ; Postal address: École Centrale de Lille, Cité Scientifique CS 20048, 59651 Villeneuve d'Ascq, France

**Abstract** A polycrystalline recrystallized $\alpha$-Fe specimen was subjected to monotonic tension up to 2 % strain. Local strain was measured all over the width of the specimen thanks to in-situ optical-based Digital Image Correlation with adequate spatial and temporal resolution. With additional knowledge of local crystallographic orientation thanks to EBSD scan before the test, strain heterogeneities and localizations were analyzed in depth. A downscaling global to local strategy was employed. At the local scale, the displacement gradient tensor was projected onto every potential slip system for fine investigation of slip activity. The results indicate that the strain structure develops at a scale larger than the grain's and leads to strain localizations around grain boundaries. The analysis of the build-up of the plastic deformation pattern has been differentiated from the one of the occurrence of strain localizations. Firstly, no correlation is found between the plastic structure and grain size but a weak one is found with grain orientation; the major influence of grain interactions has been discussed. Secondly, strain localizations are observed when several slip systems are activated simultaneously in a reduced area.

**Keywords** Grain boundaries (A) - Microstructures (A) - Polycrystalline material (B) - Mechanical testing (C) - Ferrite

**COLOR SHOULD BE USED FOR ALL FIGURES IN PRINT**

# 1 Introduction

Ferrite ($\alpha$-Fe phase) is present in all low-carbon steels. It constitutes the microstructure in Interstitial-Free steels, widely used in the automotive industry for their good formability. Besides, it serves as the ductile matrix of many bi-constituent steels, such as ferrite-pearlite steels used in the railway industry. It is well known that, as in every polycrystal, the deformation of an aggregate of heterogeneous ferrite grains leads to strain heterogeneities and localizations at the scale of the microstructure. These heterogeneities build-up early on, even in single-phase polycrystals under monotonic uniaxial loading. They arise from the interactions between the elastically and plastically anisotropic crystals [1]. Understanding the development of these heterogeneities is of paramount importance when the lifetime of a component strongly depends on its microstructural features [2, 3]. The build-up of these heterogeneities and the occurrence of plastic localization is not yet fully understood in polycrystals, let alone in ferrite.

Previous studies of polycrystalline ferrite under monotonic uniaxial tension, at room temperature and in quasi-static conditions, have highlighted strain heterogeneities from the beginning of the elastic-plastic transition, both between grains and inside grains [4–7]. With Digital Image Correlation (DIC), these heterogeneities were measured even before the start of the macroscopic yielding [8]. Tomota et. al. have split the monotonic deformation into three macroscopic stages: the elastic domain, where strain is nearly homogeneous, then the individual yielding of the grains, as a function of their orientation, and finally the so called "stage III" plastic deformation of the aggregate, characterized by the continuous increase of dislocation density [9]. The spatial distribution of strain heterogeneities is determined at the beginning of the deformation and does not change with increased loading [10]. Even though these heterogeneities develop at a scale that is larger the grain's [11, 12], they lead to significant strain localizations, which are mostly captured next to and along grain boundaries [5, 6, 10], where high local stress is found [11, 13]. Both the elastic and plastic anisotropy of the grains are known to contribute to the heterogeneous distribution of stress [14]. However, the influence of the initial orientation of a given grain is not clear. Allain-Bonasso et. al. did not find any correlation between the grain orientation spread, a measurement of local misorientation with Electron BackScatter Diffraction (EBSD), and several grain parameters, including the maximum Schmid factor [15]. Similarly, no correlation was found with the local plastic strain, even though only a limited number of grain was considered [16]. Oddershede et. al., who have investigated the behavior of a few bulk grains by 3D X-Ray Diffraction, claim that the initial orientation determines the most active slip systems [17]. They also acknowledge that the remaining slip activity depends on the interactions with neighboring grains. In a complementary study, the same team highlights the role of long-range interactions, with the evidence that different lattice rotation paths have been measured for two grains with similar orientation, size, shape and environment [18].

Additional studies, that deal with plasticity in other single-phase polycrystalline Body-Centered Cubic (BCC) structures under monotonic tension, have also attempted to understand plastic heterogeneities. In a polycrystalline titanium specimen, [100]-oriented grains (w.r.t. the tensile direction) were found to show the largest tendency for local orientation change, as opposed to the [110]-oriented grains [19]. This was explained on the basis of the number of highly-stressed slip systems, i.e. the initial Schmid factors. In a polycrystalline tantalum specimen, misorientation measurements showed that significant orientation gradients formed near the initial grain boundaries, leading to the fragmentation of the parent grain into several smaller subgrains [20]. In the same material, no influence of the grain size was recorded but a "modest" correlation was found between the initial maximum Schmid factor and the grain-averaged plastic strain [21]. The correlation is slightly improved by grouping similarly oriented neighboring grains, and is significantly higher in an oligocrystalline specimen with columnar grains in the through-thickness. It is

concluded that the neighboring effects from surrounding grains must be taken into account [22]. As a consequence, several experiments have been dedicated to the measurement of heterogeneities in the bulk of a polycrystalline titanium specimen under tension [23–25]. In these studies, the influence of the grain environment was detailed: the Zener anisotropy ratio was mentioned to significantly affect the grain-scale strain and stress distributions, even beyond yielding. Besides, significant rotation of the grain-averaged stress tensors occurs during the elastic-plastic transition, because of both the external loading and surrounding grains. These experiments allow for a statistically representative grain-scale information, both in the bulk and in surface, but fail to address the grain-to-grain yielding transition. More data is found in Face-Centered Cubic (FCC) materials [26–36], where slip analysis is easier.

A key difference in BCC structures is that at room temperature and in quasi-static conditions, slip is mainly governed by the motion of low-mobility screw dislocations, which are not confined to a single plane [37]. As a result, anomalous slip is reported where Schmid's law is violated [38]. Besides, there is no close-packed plane, and therefore dislocations are susceptible to glide onto any plane that contains a <111> direction, such as {110}, {112} or {123} planes [39]. Non-crystallographic slip has also been observed where dislocations glide onto the potentially non-crystallographic plane with the maximum resolved shear stress [40]. Finally, cross-slip is often reported where dislocations move from one plane to another and leave curved marks on the surface, known as "pencil glide" [41]. In $\alpha$-Fe, recent investigations of slip in ferrite single-crystals suggest preferential slip on the {110}<111> and {112}<111> slip systems, at room temperature and in quasi-static conditions [42]. Other studies have clarified that, even though the slip plane is on average of the {112} family, slip marks are formed of short but straight {110} elementary slip [43, 44].

The previously discussed strain heterogeneities in $\alpha$-Fe, which are measured at the microscopic/mesoscopic scale, and influence the macroscopic behavior of the material, are a direct consequence of the deformation mechanisms at the lattice scale. Therefore, it is obvious that a multiscale strategy, that gathers in-situ accurate strain measurement and slip identification all over a representative surface, is required. Such experiment is complex to produce because either (i) only a small non-representative part of the specimen is observed, typically several hundreds of micrometers squared, (ii) the spatial resolution of the measurements is not fine enough with regard to the microstructure, (iii) images are not recorded continuously during the test or (iv) slip systems are not identified. For instance, in high-resolution DIC studies inside a Scanning Electron Microscope (SEM) such as some of the references mentioned above, kinematics measurements cannot be performed along the entire width of the specimen under deformation, and any further dialogue with numerical simulations is biased by strong hypotheses.

To our knowledge, no experiment that addresses all four previous constraints has been performed so far. Therefore, the present work aims to produce, at the scale of the microstructure and along the entire width of an $\alpha$-Fe polycrystalline specimen, continuous and accurate strain measurements during the monotonic tension of the said specimen, where the active slip systems are identified throughout the deformation. Strain heterogeneities and localizations on the surface of the specimen, which have been measured with DIC, are analyzed and discussed with regard to previous studies. To do so, a downscaling global to local analysis approach is employed, and slip identification is carried out in an original manner by projecting the kinematics measurements onto crystallographic directions. In addition, the surface of the specimen after deformation was characterized with optical microscopy, optical profilometry and orientation imaging (EBSD detector).

# 2 Material and methods

## 2.1 Experimental procedure

The material used is ARMCO 99.9 % pure Iron (0.001C - 0.004Si - 0.05Mn - 0.003P - 0.003S - 0.015Cr - 0.009Cu - 0.002Mo - 0.014Ni - 0.002Sn, in weight fraction). A small dogbone tensile specimen (reduced cross-section equal to $5 \times 2.5$ =12.5 $mm^2$, overall length equal to 46 mm) has been cut by electrical discharge machining from a recrystallized sample. The recrystallization process was performed to coarsen the grain size and facilitate the measurements. It consisted in 1 % deformation followed by 1 h annealing treatment at 800°C. The surface of the tensile specimen was mechanically polished down to 1 µm diamond suspension then oxide polished for 30 min. A 32 $mm^2$ region of interest was delimited by four small Vickers indents. They will serve as fiducial markers for data repositioning. The microstructure was characterized with optical microscopy and EBSD. A speckle pattern was applied onto the surface of interest to induce local grey level variations that are necessary for DIC. Its preparation is further detailed in the following section. A 120 Ω strain gauge was bonded onto the other face of the specimen (see figure 1). The test was carried out within a Kammrath & Weiss GmbH uniaxial tension/compression module equipped with a 10 kN load cell. It consisted in displacement-controlled monotonic tension up to 1.5 % strain followed by elastic unloading, at room temperature and at a mean strain rate of $2.5 \times 10^{-4}\,s^{-1}$. Images of the surface of interest are captured continuously during tensile testing with the digital camera presented in 2.2. All devices were connected to a T7-Pro LabJack mini-measurement laboratory for synchronizing. Internally developed CRAPPY library under Python programming language [45] was used for test management and data acquisition. After the test, the speckle pattern was removed with ultrasonic bath cleaning. Then, the deformed microstructure was characterized with optical microscopy, optical profilometry and orientation imaging (EBSD detector).

## 2.2 Digital Image Correlation

In-situ full-field kinematics measurement DIC is the core of the presented study. It is acknowledged as a straightforward and powerful tool for accurate surface measurements. It consists of computing local displacement fields by minimizing grey level differences between a reference and a deformed images. Following criteria must be ensured for measuring the formation of strain heterogeneities at the microstructure scale:

- *High spatial resolution:* The measurement pitch should be as fine as possible with regard to microstructure features so that local strain variations are captured.
- *High measurement accuracy:* Accurate measurements are required for future dialogue with numerical simulations. All error sources such as matching error, sensitivity to out-of-plane movements, lens distortion and overall noise must be minimized.
- *Preservation of specimen free-surfaces:* Displacement fields are to be measured along the entire width of the specimen for optimal further dialogue with numerical simulations.
- *Temporal tracking:* Images must be continuously recorded in order to monitor the temporal evolution of the deformation structure.

The preservation of the free-surfaces of the specimen and the temporal tracking have motivated the choice of in-situ optical-based DIC. Despite the coarser spatial resolution, microscale measurements can be achieved with optical-based DIC [46, 47]. The solution chosen in this work takes advantage of the grain coarsening recrystallization process. An OPTART MP-1F-65 telecentric

lens with 1.0X magnification is attached onto a XIMEA MC124MG camera with a 4112 × 3008 pixels sensor. The resulting field of view is 14.2 × 10.4 $mm^2$ with a pixel size of 3.45 µm. 4 images per second were recorded on average throughout the test.

Appropriate speckle pattern protocol must be followed to ensure the criteria presented above. Small calcium carbonate particles were dispersed in an ethanol solution. Then the solution is vaporized onto the surface of interest with an airbrush after painting a homogeneous black layer. The resulting speckle pattern is fine, dense and contrasted. Kinematics fields are computed with a global method that is based on a finite element decomposition. The associated regularization scheme allows for smaller element size than with a local subset-based method [48]. Besides, displacement fields are not spatially smoothed after computation. Instead, a median filter is applied at every stage of the downscaling DIC pyramid (the filter radius is chosen equal to a minimum value of 3). This ensures low noise while preserving local kinematics variations. The method is implemented in an internally developped YaDICs platform [49, 50]. Axial strain $\epsilon_x$ and transverse strain $\epsilon_y$ are computed after numerical gradient of in-plane displacement fields (infinitesimal strain theory is assumed). Shear strain is equal to $\epsilon_{xy} = \frac{1}{2} \times (\frac{\partial u}{\partial y} + \frac{\partial v}{\partial x})$ and in-plane rotation is equal to $\omega_{xy} = \frac{1}{2} \times (\frac{\partial v}{\partial x} - \frac{\partial u}{\partial y})$. The von Mises equivalent strain is computed with the following formula: $\epsilon_{vm} = \sqrt{\frac{4}{9}(\epsilon_x^2 + \epsilon_y^2 - \epsilon_x \epsilon_y) + \frac{4}{3}\epsilon_{xy}^2}$. All strain fields computed with YaDICs are in the reference framework, i.e. the coordinate system of the reference image.

In-plane and out-of-plane rigid-body (RB) translations have been carried out before the test for strain uncertainty estimation. They allow for assessment of the whole measurement chain even though it should be kept in mind that they only induce homogeneous kinematics fields. The in-plane RB translation corresponds to a homogeneous displacement of about 100 µm in both axial and transverse directions. The magnitude of the measured displacement vector is equal to 46.4 pixels which is higher than the highest local displacement magnitude measured during the tensile test. The out-of-plane RB translation corresponds to a displacement of about 100 µm in the out-of-plane direction. The actual amount of out-of-plane motion during the test is unknown. It can result from parallelism fault, specimen realignment and out-of-plane deformation. Tab. 1 presents the mean and standard deviation values of von Mises strain as a function of DIC element size after both in-plane and out-of-plane RB translations. The closer to zero the measured strain, the lower is the measurement error. Both mean and standard deviation values decrease with increasing element size. This illustrates the inevitable compromise between spatial resolution and measurement accuracy in DIC. More interestingly, the values drop down to noise values when the element size is large enough. It means that the error induced by RB translations is mainly due to matching and the measurement chain is only slightly sensitive to out-of-plane movements. This comes from the telecentric feature of the lens.

| Element size | In-plane translation | Out-of-plane translation |
|---|---|---|
| 8x8 pixels | $729 \pm 428$ | $768 \pm 466$ |
| 16x16 pixels | $287 \pm 167$ | $310 \pm 179$ |
| 32x32 pixels | $181 \pm 114$ | $66 \pm 41$ |

Table 1: Mean and standard deviation values of von Mises equivalent strain field in the region of interest after in-plane and out-of-plane rigid-body translations, as a function of the element size used for computation. Strain values are expressed in microstrain.

Besides the finite element-based global method, YaDICs also features a homogeneous method

that basically acts as a video-extensometer and returns the macroscopic axial strain $E_x$[1]. This homogeneous method is not subjected to errors arising from local correlation but remains affected by errors that come from the optical chain, such as out-of-plane motion. The macroscopic stress-strain curve is plotted in Fig. 1. The strain measured with YaDICs homogeneous method is compared to the strain returned by the strain gauge. Good agreement is observed until $E_x \approx 0.5\,\%$. This further confirms the good accuracy of the measurements. Beyond that value, the strain from the gauge is lower than the value from YaDICs homogeneous method; the difference keeps increasing until the final elastic unloading. This difference is explained by the small size of the gauge ($1\times0.7\,\mathrm{mm}^2$) compared to the characteristic size of the microstructure, which is presented in Fig. 2. It is likely that the strain returned by the gauge corresponds to the plastic deformation of a few grains in the back face of the specimen, and hence might not be representative of the mean strain on the front face.

All further local DIC measurements presented in this paper were computed with YaDICs finite-element based global method 16x16 pixels ($\approx$ 55x55 $\mu\mathrm{m}^2$) element size. It minimizes the matching error without sacrificing spatial resolution. On the one hand, kinematics measurements are expected to be accurate and the resulting measurement pitch is about 7 times lower than the mean grain size, characterized in the following subsection. In addition, it is reminded that an image is recorded approximately every $7 \times 10^{-5}$ strain increment. On the other hand, only in-plane strain can be detected, and the spatial resolution of the measurements is not fine enough to capture displacement discontinuities induced by slip events [36]. As a consequence, the measured strain values depend on the element size, and therefore cannot be considered as quantitative.

## 2.3 Microstructure characterization

This study features microstructure observation with optical microscopy, crystallographic orientation determination with EBSD and surface height measurements with optical profilometry. All data (both before and after tensile testing) can be transformed back into the reference framework of DIC by using Vickers fiducial markers and computed displacement fields. Accurate repositioning has been checked.

**Optical microscopy and profilometry** NIKON Eclipse MA200 optical microscope with DS-Fi2 camera was used at X50 overall magnification in bright field mode for microstructure observation before and after tensile testing. NIS-Elements software allowed stitching of micrographs with 20 % overlap area for reconstruction of the whole surface of interest with a pixel size of 680 nm. Note that some unfortunate scratches remained on the surface after polishing. They were identified thanks to the micrograph captured before testing. (supplementary_material_figure_A.pdf)

Height measurement was performed only after tensile testing as the initial surface is assumed to be flat thanks to diamond and oxide polishing. VEECO Wyko NT1100 optical profilometer was used at X5 overall magnification in Vertical Scanning Interferometry mode. Corresponding software was Wyko Vision. Likewise, stitching with 20 % overlap area was performed to cover the whole surface of interest. The measurement pitch is 1.6 µm. Tilt term was removed by plane fitting in order to focus on surface roughness.

**Electron backscatter diffraction** Local crystallographic orientation was obtained with an EBSD detector inside JEOL JSM-7100F FEG-SEM using Oxford Instruments AZtecHKL software. The acceleration voltage was 15 kV, the working distance was 20 mm and the specimen

[1] In this manuscript, the macroscopic strain is written with the capital letter $E_x$, so that it is differentiated from the local strain $\epsilon_x$. In order to match this notation, the macroscopic stress computed from the load given by the load cell is written $\Sigma$.

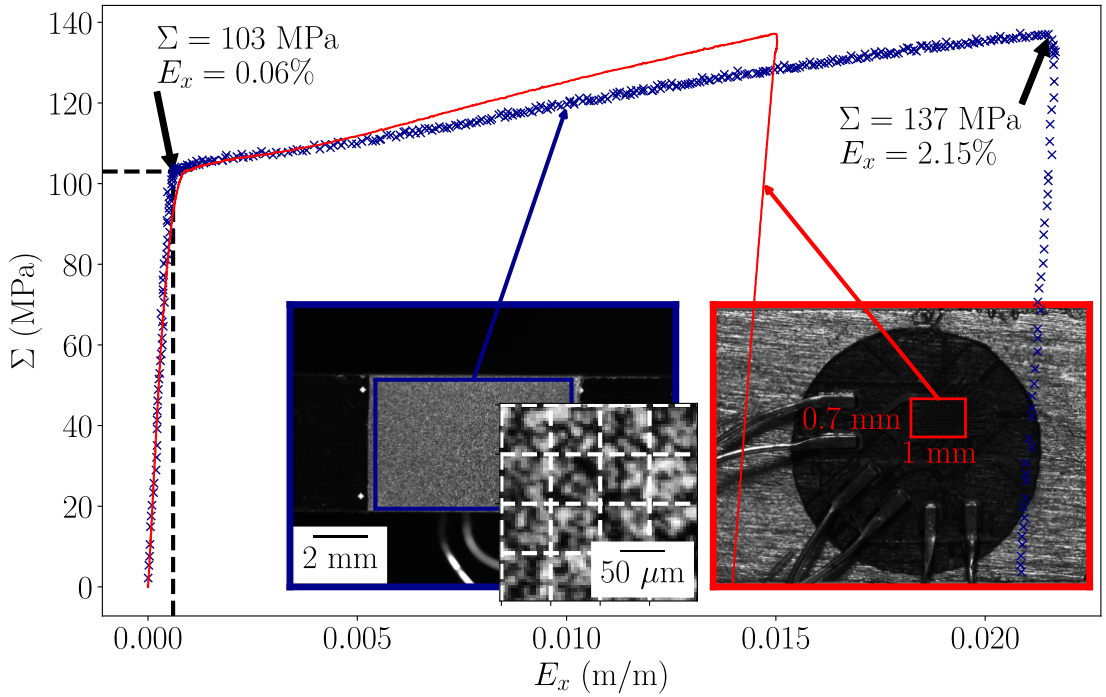


Figure 1: Macroscopic stress-strain curve. Stress is computed after the load value obtained from the load cell. Strain is measured by Digital Image Correlation (dark blue X markers) and strain gauge (red solid line). The left image displays the measurement reference image as seen by the optical device. The dark blue rectangle corresponds to the region of interest shown in Fig. 2. A magnified image of the speckle pattern is also shown with a superposed grid of 16x16 pixels ≈ 55x55 µm$^2$. The right image displays a magnified image of the back face of the specimen. The red rectangle corresponds to the attached strain gauge with length 1 mm and width 0.7 mm.

was 70° tilted. The surface of interest before testing was covered with two scans at X20 magnification with 3 µm pitch. Image distortions are significative at such low SEM magnification [51]. They have been removed using Thin Plate Splines transformation [52]. In practice, the transformation was determined by finding about fifty to one hundred correspondence points between DIC framework and EBSD scan. Stitching was performed using OpenCV library under Python programming language. A similar procedure was conducted after tensile testing except that only one scan was performed. The scan covers 71 % of the surface of interest.

The virgin microstructure, repositioned in the reference framework of DIC, is presented in Fig. 2a. It is segmented into 242 grains from the EBSD scan performed before the tensile test. The corresponding grain boundary network will be used to analyze DIC strain fields with regard to the microstructure. The mean grain size, as characterized by the maximum Feret diameter, is equal to 419 µm. The corresponding yield stress derived from Hall-Petch relationship with this value is equal to 103 MPa (Hall-Petch law parameters were identified on the same material in [53]). This is in good accordance with the measured yield stress that was presented in Fig. 1. Nevertheless, this agreement might be a coincidence since the grain size distribution, displayed in Fig. 2b, is bimodal. In particular, a high number of grains show a diameter equal to about

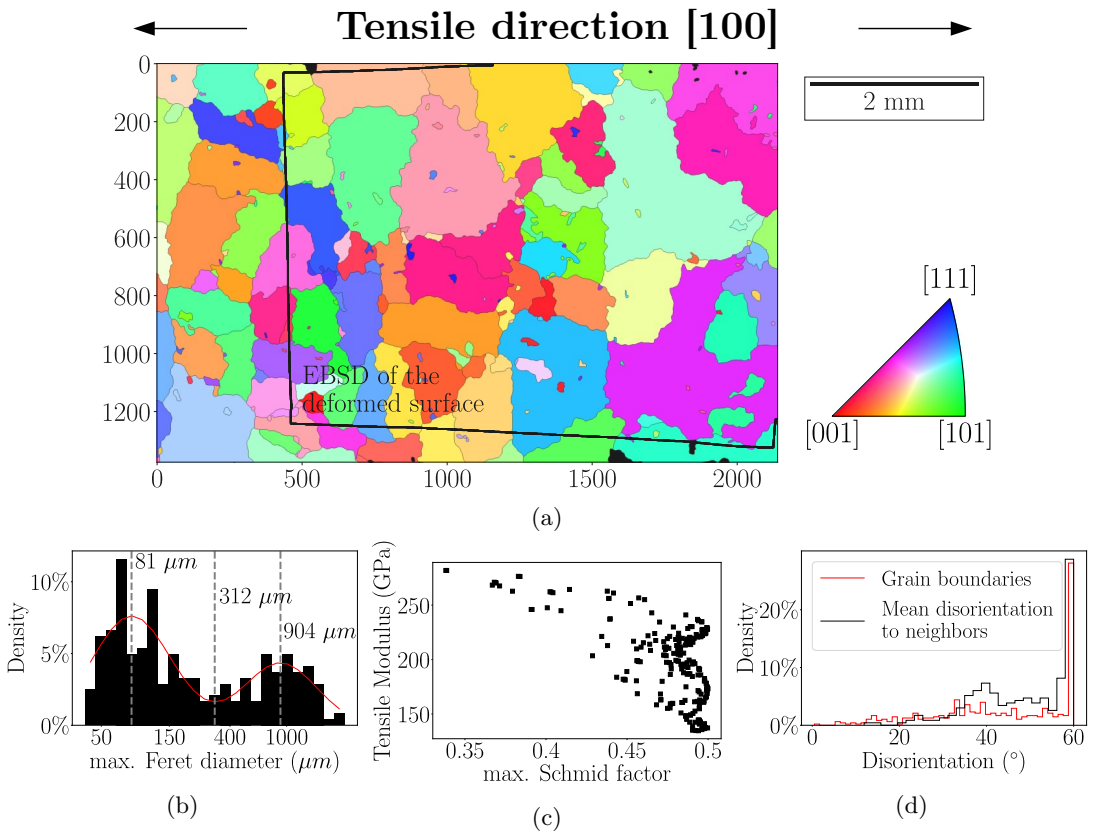


Figure 2: (a) Inverse Pole Figure (IPF) mapping (with regard to [001] direction) of the microstructure in the surface of interest that has been repositioned in the reference framework. Color coding is explained by the IPF unit triangle. Grains in black refer to unknown orientation. The area that was scanned again with EBSD after the test is delimited by the black lines. X and Y axes are expressed in pixels. (b) Corresponding bimodal grain size distribution (expressed by the maximum Feret diameter). (c) Maximum Schmid factor and Tensile modulus of all grains in the surface of interest. (d) Distribution of disorientation at grain boundaries and with respect to neighboring grains.

80 µm. Many of them seem to be encapsulated in larger grains, whose diameter reaches up to 1 mm. This bimodal distribution is likely to be the consequence of the recrystallization process.

Besides segmentation, the initial EBSD scan provides local crystallographic orientation through Euler angles $\phi_1$, $\Phi$, $\phi_2$. The rotation matrix from the sample coordinate system to a given grain coordinate system can be derived, as recalled in appendix A. It allows computation of crystallographic criteria in order to analyze the individual deformation of the grains. For example, the tensile modulus, which is the elastic modulus of a given crystal with regard to the tensile direction, has been computed for each grain to account for the elastic anisotropy. Its definition is reminded in appendix A. The mean tensile modulus in the region of interest is equal to 198 GPa which agrees well with the fitted macroscopic Young's modulus from Fig. 1, equal to 193 GPa. In addition, the Schmid factor of all {110} and {112} slip systems have also been computed in each grain, and the maximum Schmid factor is used to investigate the onset of plastic activity. The latter is greater than 0.4 in 94 % of the grains, because of the large number of slip systems

in BCC materials. Note that grains with high Schmid factor tend to have low tensile modulus, as highlighted in Fig. 2c. Finally, the disorientation between two grains, i.e. at a grain boundary, can also be calculated from the rotation matrices of the two grains considered. In order to study the environment of the grains, it is proposed to deduce the mean disorientation to neighboring grains. For each grain, the latter is obtained by weighting the disorientation values of the grain boundaries according to the length of these same boundaries. The calculations are all detailed in appendix A. The distributions of the disorientation at the boundaries and the average intergranular disorientation are presented in figure 2d. The distribution reaches a first peak around 40°, which is expected in a non-textured cubic polycrystal [54]. However, nearly 30 percent of the grain boundaries have a disorientation of about 60°. These high disorientations are observed between the small encapsulated grains and the corresponding large grains. Again, this feature is probably a consequence of the recrystallization process.

# 3 Results and discussions

## 3.1 Strain fields measured with Digital Image Correlation

The evolution of the von Mises strain $\epsilon_{vm}$ with overlaid grain boundaries is presented in the online version (supplementary_material_video_A.mp4). A few moments are displayed in Fig. 3. During early elastic domain, the signal is dominated by noise. A first localization is spotted on a grain boundary shortly before macroscopic yielding at $\Sigma \approx 85\,\text{MPa}$ (Fig. 3a). Then, a second localization crosses a few grains (Fig. 3b), right before the macroscopic yielding that takes place from $\Sigma = 103\,\text{MPa}$ and $E_x = 0.06\,\%$. These localizations are highlighted by blue ellipses in the figure. The first localization accumulates strain during loading (it ultimately records high $\epsilon_{vm}$ value in Fig. 3f), as opposed to the second one, which is no longer observed in Fig. 3e. In both cases, nearby plastic activity is triggered, and the second localization is followed by plastic strain heterogeneities that quickly diffuse from the left to the right part of the specimen (Fig. 3c). A steady plastic deformation pattern is drawn whose scale is larger than the grain's. Shortly after its build-up, significant plastic localizations are observed at a more local scale (Fig. 3d). Finally, strain accumulates at the localizations, i.e. their intensity monotonously increases with macroscopic strain and the spatial distribution of strain is preserved until the end of the test (Fig. 3e and 3f). From these observations, it seems that the strain localizations at the end of the test are the result of local strain accumulation in areas that were part of the plastic deformation pattern that takes place in the first time, and whose scale is larger than the grain's. Therefore, given the discrepancy in time occurrence and scale, the initial build-up of the plastic deformation pattern should probably be differentiated from further local strain accumulation, which leads to strain localizations.

In order to take a closer look at strain localizations, Fig. 4 details more specifically the corresponding strain and rotation components $\epsilon_x$, $\epsilon_y$, $\epsilon_{xy}$ and $\omega_{xy}$ after the elastic unloading, i.e. at the end of the test ($E_{x,U} = 2.09\,\%$ where U stands for Unloading). Since the spatial distribution of strain is stable in most parts throughout the plastic domain, strain fields at $E_{x,U} = 2.09\,\%$ are representative of what happened during loading. Measured strain is heterogeneous both between and inside grains. Axial strain field shows strain localizations mostly next to grain boundaries and at triple junctions. Great scatter is observed as some grain boundaries, highlighted by blue rectangles in Fig. 4a, show intense deformation while others, highlighted by cyan rectangles, seem to deform quasi-elastically. The boundaries that record high axial strain also often undergo a lot of rotation (Fig. 4d). Another interesting area, highlighted by the solid blue circle in Fig. 4a, shows axial strain circling around a small grain. This same area records both clock-wise

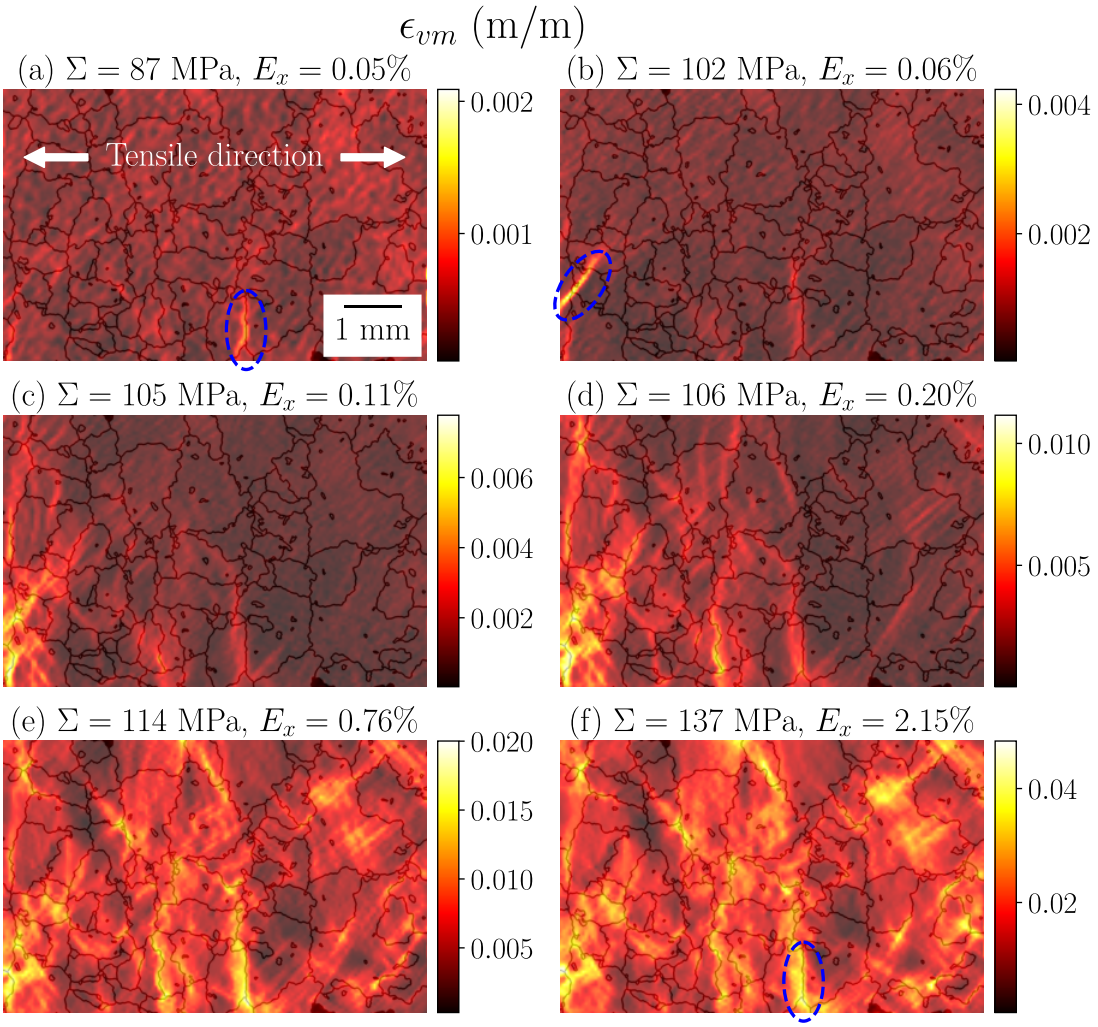


Figure 3: Evolution of local von Mises strain $\epsilon_{vm}$ with increasing loading, superposed on the grain boundary network. (a) First localization before macroscopic yielding, (b) Onset of macroscopic yielding, (c), (d), (e) and (f) plastic domain. Elliptic patches highlight areas of interest that are detailed in the text.

and anti-clockwise rotation (Fig. 4d), large compression transverse strain (Fig. 4b) and high shear strain (Fig. 4c) around the faintly deformed grain. These are the consequence of the accommodation of the inhomogeneous deformation. Concerning strain accommodation, positive transverse strain is measured locally, as highlighted by the dotted blue circles in Fig. 4b, even though macroscopic transverse strain is of course negative. Similarly, the magnitude of shear strain is higher than axial strain in a localized area below a boundary, highlighted by the dotted cyan circles in Fig. 4a and 4c. These behaviors are likely to originate from complicated local stress state that is imposed by neighboring grains. These observations can be summarized as follows: i) grain boundaries and triple junctions seem to represent preferential sites for strain localizations, and ii) interactions with nearby grains undergoing deformation play a role in strain

heterogeneities. Both points agree with previous studies discussed in the introduction.

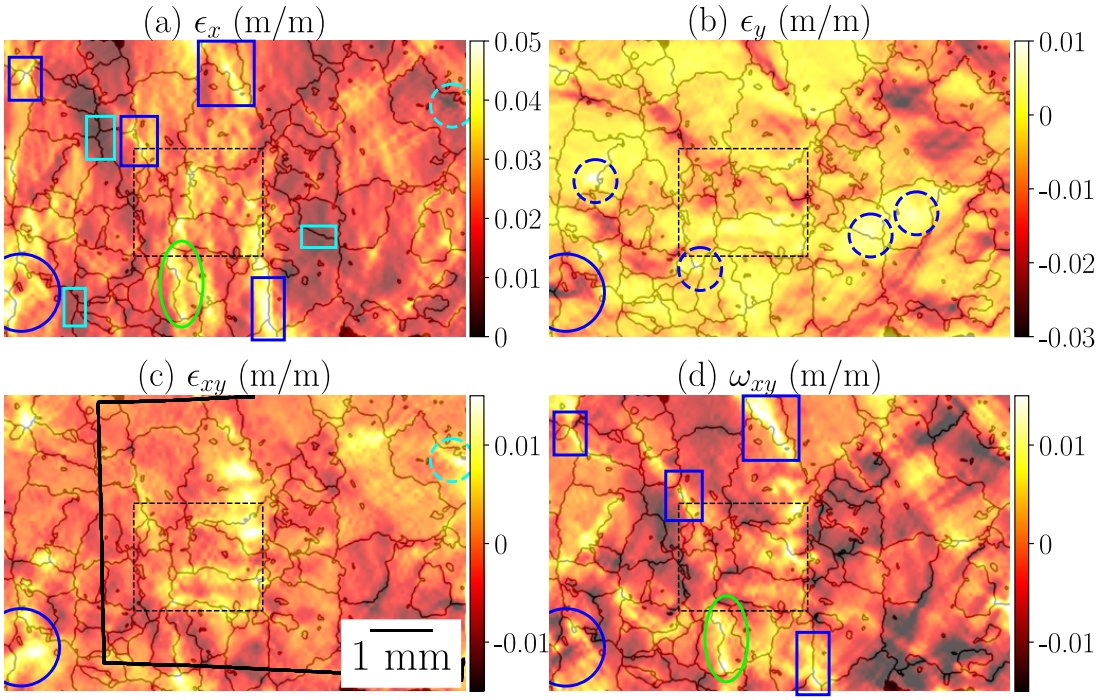


Figure 4: Focus on strain and rotation fields after elastic unloading ($E_{x,U} = 2.09\,\%$), superposed on the grain boundary network. (a) Axial strain $\epsilon_x$, (b) Transverse strain $\epsilon_y$, (c) Shear strain $\epsilon_{xy}$ and (d) In-plane rotation $\omega_{xy}$.
Blue/cyan circular and rectangular patches highlight areas of interest that are detailed in the text. The dashed black rectangles correspond to the magnified area presented in Fig. 5b. In subfigure (c), the inside of the solid black lines corresponds to the EBSD scan of the deformed surface and resulting computation of $\Theta$ presented in Fig. 5c. Finally, the green elliptic patches in subfigures (a) and (d) correspond to the one in Fig. 5c.

## 3.2 Characterization of the deformed surface

Firstly, the deformed surface, which is the surface of the specimen after tensile testing ($E_{x,U} = 2.09\,\%$), was investigated with optical microscopy. A magnified area of the optical micrograph is shown in Fig. 5a. Slip activity is heterogeneously observed even at the scale of individual grains. Many areas show intense and multiple slip marks while others appear undeformed. The deformed areas show good correspondence with the strain localizations previously presented. Besides, a great variety of marks is observed including straight, curved, wavy, fine and coarse marks. Grain boundaries often delimit marks with different angles, even though some of them are not deviated. Deformation twinning is not observed, as confirmed by EBSD. These observations imply that deformation by slip was the main mechanism during the test. Nevertheless, it is acknowledged that the presented characterization methods cannot distinguish slip close to boundaries from grain boundary sliding.

As presented in the introduction, the curved feature of observed slip marks is typical of BCC

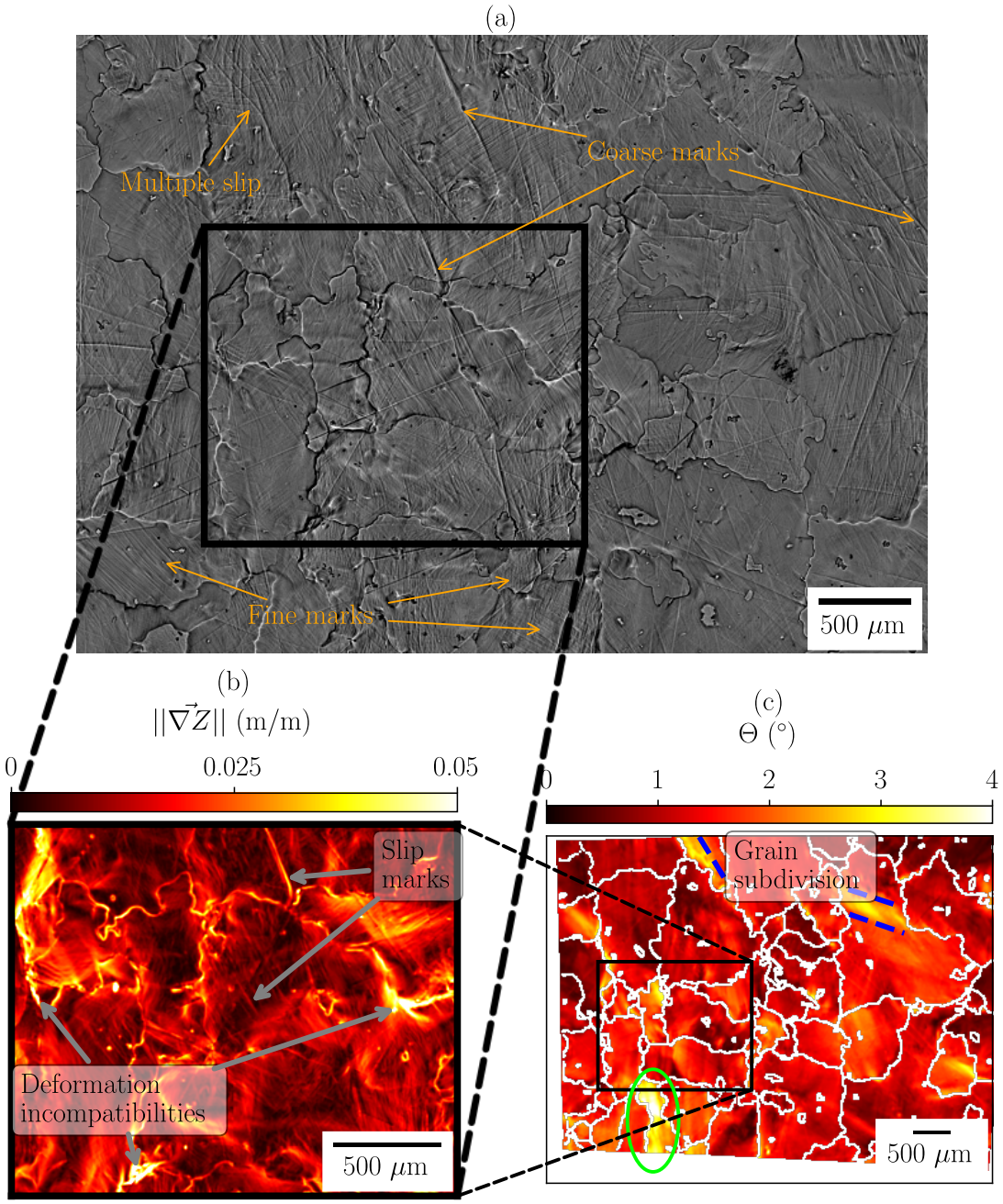


Figure 5: Characterization of the deformed surface, after the end of the test: (a) Magnified image of the optical micrograph revealing slip marks. Contrast has been slightly enhanced for better visualization. (b) $||\vec{\nabla}Z||$ (magnitude of the gradient of out-of-plane displacement); only a magnified area is shown. The location of the latter on the region of interest is drawn by the blue rectangles. (c) $\Theta$ (Grain Initial Orientation Deviation) with superposed grain boundary network. $\Theta$ has been computed wherever the crystallographic orientation of the deformed surface is known (see Fig. 2). The green elliptic patch corresponds to the ones in Fig. 4a and 4d.
All images are repositioned in the reference framework.

materials. Such marks, which result from the combination of several glide planes, are commonly referred to as "pencil glide". They highlight the complexity of identifying the activated slip systems during the test. Nevertheless, under the assumption that slip occurs along crystallographic planes, it is possible to estimate active slip planes on a mesoscopic level based on slip marks as seen by the optical micrograph. For a given slip mark, the angle between the mark and the loading direction (horizontal axis) is measured. With knowledge of the crystallographic orientation of the grain where the mark lies, the measured angle can be compared to the theoretical angles associated to each of the 48 slip systems among <111>{110}, <111>{112} and <111>{123} [55]. The computation of the theoretical angles is detailed in appendix A.

This strategy has been carried out manually within 45 grains. The grains were chosen randomly and are expected to be representative of the whole surface of interest. A total of 162 slip systems has been identified (supplementary_material_figure_B.pdf). The distribution of the number of activated systems per grain, which is similar to the one simulated in [12], displays between 2 and 6 active systems per grain. This number usually increases with the size of the investigated grain. In most grains, there are one or two slip systems that exhibit marks in almost the entire grain. These systems seem to contribute to most of the deformation of the grain. Remaining marks are only found locally, in particular next to grain boundaries and triple junctions. They correspond to systems that are expected to be activated as a consequence of neighboring grains. Finally, the proportion of {110}, {112} and {123} systems is 56 %, 30 % and 14 % respectively.

It is acknowledged that the presented slip analysis shows several limits. First, the assumption that slip occurs along crystallographic planes has not been verified; instead, slip could have followed the maximum resolved shear stress plane [40]. Secondly, it is possible that a given slip mark cannot be associated unambiguously to a single slip system. In that case, the selected system has been chosen as the one with the maximum Schmid factor. This is another strong assumption [38], especially near grain boundaries. Finally, the active planes identified as {112} or {123} type could be formed of {110} elementary slip at a smaller scale [43, 44], which cannot be resolved with optical slip trace analysis. Yet, this scale is not captured either by the presented DIC measurements, and therefore it is legitimate to consider the "apparent" slip planes identified at the mesoscopic scale. In that regard, with a similar analysis, slip was found to occur only along "apparent" {110} and {112} planes in $\alpha$-Fe single-crystals, at room temperature and in quasi-static conditions [42, 44]. Therefore, in the presented study, it will be assumed that slip has occurred along {110} and {112} planes.

Secondly, out-of-plane motion during the test was investigated by optical profilometry. The output is the local height $Z$ of the deformed surface. The latter is arbitrarily centered around 0 and ranges from -10 to 10 µm. In order to better correlate the local out-of-plane displacement to the microstructure, $Z$ is derivated along X and Y axes. The resulting field is the magnitude of the gradient of the out-of-plane displacement $||\vec{\nabla Z}|| = \sqrt{(\frac{\partial Z}{\partial x})^2 + (\frac{\partial Z}{\partial y})^2}$. Its dimension is the same as strain. A magnified area is shown in Fig. 5b. The computed field is particularly localized. It clearly reveals grain boundaries where out-of-plane motion is measured. In addition, most slip marks are also visible as they produce a small out-of-plane step on the surface. Therefore, the heterogeneous plastic deformation of the microstructure was accompanied by noticeable out-of-plane motion, which meets the results presented in the literature [3, 56, 57]. Besides, strain localizations measured with DIC do not necessarily correspond to areas with high $||\vec{\nabla Z}||$ and inversely. As a consequence, the local kinematics is not fully described by 2D information obtained from DIC.

Finally, the deformed surface is investigated by EBSD for potential crystallographic rotation resulting from tensile deformation. The IPF mapping in the direction normal to the surface (not presented here) presents small deviation in coloring but remains mainly similar to the corresponding deformation-free map. It suggests moderate lattice rotation. It is expected since the macroscopic strain at the end of the test is low ($\approx 2\,\%$). To better characterize the local lattice rotation, the Grain Initial Orientation Deviation $\Theta$ is computed for every pixel of the reference framework. It represents the disorientation angle between the crystallographic orientation before and after the test (see appendix A for more details). Hong et. al. have successfully used this metric to investigate deformation in a magnesium alloy at low plastic strains [58]. Besides, it allows a direct comparison between undeformed and deformed EBSD scans. The resulting field $\Theta$ is presented in Fig. 5c. It is also highly localized and ranges from 0° to more than 5°. The mean value is equal to 1.3°. Highest values are mostly measured next to grain boundaries. This can be explained on the basis of a higher density of Geometrically Necessary Dislocations [59], resulting in local lattice rotation [60]. Furthermore, a correlation between strain localizations and lattice rotation has been investigated: higher values of $\Theta$ are globally associated to greater strain measured with DIC (supplementary_material_figure_C.png). An illustration of this result is the grain circled in green in Fig. 4a, 4d and 5c that shows significant lattice rotation as well as high axial strain and in-plane rotation. Last but not least, some distinct patterns suggest early signs of grain subdivision, i.e. some grains subdivide into portions with different crystallographic orientation, as highlighted in the previously mentioned figure. This phenomenon is known to be the consequence of the interactions with neighboring grains [17, 18, 28]. This confirms the major role of grain environment in the presented strain heterogeneities.

In the following subsections, it will be attempted to further investigate the build-up of the plastic deformation pattern and the occurrence of strain localizations by using a downscaling strategy, i.e. from a global to a local approach.

### 3.3 Global investigation of strain heterogeneities and localizations

In a first approach, a statistical analysis of the measured strain distributions is proposed. The surface of interest is split into intragranular and intergranular domains (as illustrated in supplementary_material_figure_D.pdf). The intergranular domain corresponds to dilated grain boundaries. The kernel of the morphological operation has been chosen to match the spatial resolution of the kinematics measurements (16 pixels wide). The resulting grain boundaries domain accounts for 10 % of the surface of interest. Several quantiles of $\epsilon_x$, $\epsilon_y$, $\epsilon_{xy}$ and $\omega_{xy}$ distributions are computed in both intragranular and intergranular domains for each image acquired during the test. The corresponding evolutions are plotted in Fig. 6, up to $E_x = 1\,\%$ for better visualization. The main difference between intragranular and intergranular domains is found when looking at the quantiles $Q_{0.9}$ and $Q_{0.1}$. In particular, the greatest 10 % of $\epsilon_x$ and $\omega_{xy}$ distributions are higher in the intergranular domain than in the intragranular domain. Similarly, the lowest 10 % of $\epsilon_{xy}$ and $\omega_{xy}$ distributions are lower in the intergranular domain. It means that the extreme values of axial strain and in-plane rotation fields are higher in absolute value in the intergranular domain than in the intragranular domain. This observation can be summarized by the von Mises strain distribution at the end of the test (not presented here), which is more right-skewed in the intergranular domain (skewness equal to 0.64) than in the intragranular domain (skewness equal to 0.52). However, the statistical difference between the two domains remains relatively small, whereas the strain fields at the end of the test suggested a bigger gap. In reality, the strain localizations measured at the grain boundaries tend to overflow into the intragranular domain, as highlighted by the blue rectangles in Fig. 4. It is therefore likely that

it is not the grain boundaries themselves that undergo deformation, but rather that they are causing the deformation in the grains (e.g., by inducing a higher local stress [13]). The spatial resolution of the kinematics measurements presented in this work does not allow us to ensure this with certainty. Nevertheless, several high-resolution studies tend to confirm this hypothesis [28, 34], even though the material is different.

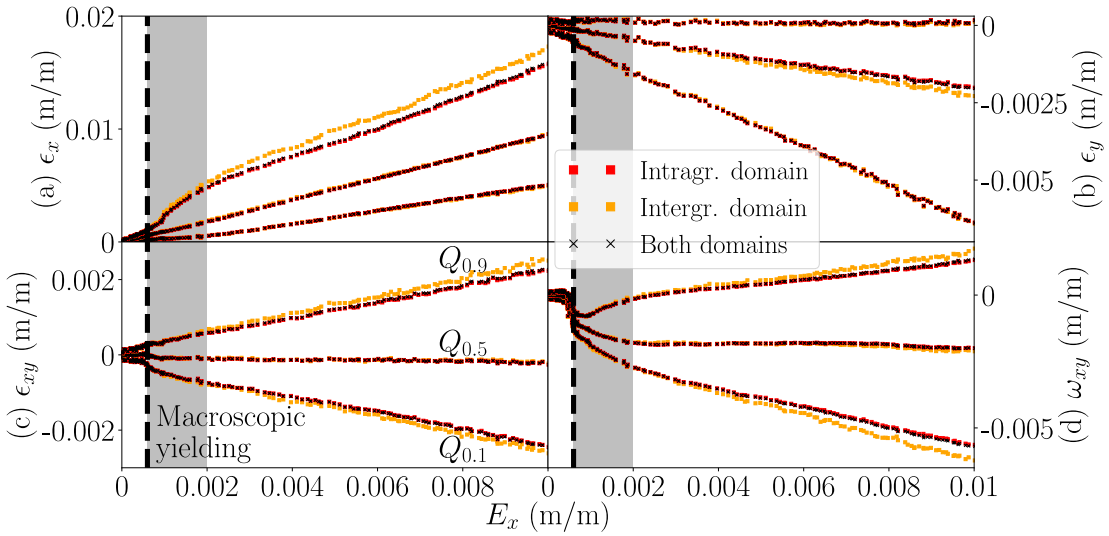


Figure 6: Evolution of several quantiles of the distributions of (a) $\epsilon_x$, (b) $\epsilon_y$, (c) $\epsilon_{xy}$ et (d) $\omega_{xy}$, up to $E_x = 1\,\%$. The presented quantiles are $Q_{0.1}$, $Q_{0.5}$, and $Q_{0.9}$, which correspond to the 1st, 5th and 9th deciles respectively (value below which 10 %, 50 %, 90 % of the distribution is found respectively). For each distribution, quantile values are computed over the whole region of interest (black), intragranular domain (red) and intergranular domain (orange). The shaded area indicates approximately the stage between the elastic regime and the strain accumulation stage.

More interestingly, the difference between intergranular and intragranular domains is not observed directly after the macroscopic yielding; it arises between $E_x = 0.2\,\%$ and $E_x = 0.4\,\%$ depending on the distribution. Then, it is enlarged with increasing loading, until the end of the test (not shown in the figure). Since this difference is associated to strain localizations near grain boundaries, it confirms that strain accumulation does not begin immediately when the macroscopic yielding takes place. Instead, it occurs later, once the plastic deformation pattern is drawn by the first strain heterogeneities. Similarly, Tomota et. al. have differentiated the "grain to grain yielding" stage, where local stress is redistributed as a consequence of misfit plastic strains, from the "stage III deformation", characterized by dislocations accumulation [9]. In our test, the "grain to grain yielding" stage would correspond to the build-up of the plastic deformation pattern, as represented by the shaded area in Fig. 6, where a non-linear variation of $Q_{0.9}$ and $Q_{0.1}$ of $\epsilon_x$ and $\omega_{xy}$ is observed. The "stage III deformation" would correspond to the strain accumulation stage that begins afterwards and lasts until the elastic unloading.

In this global analysis, the predominance of strain localizations next to grain boundaries was confirmed and the build-up of the plastic deformation pattern was differentiated from the strain accumulation stage. Nevertheless, this scale of investigation does not allow investigating the

influencing factors in the build-up of the plastic deformation pattern and the occurrence of strain localizations. It requires information obtained at least at the scale of the grains.

### 3.4 Grain-scale investigation of strain heterogeneities and localizations

In a second approach, the influencing grain-scale factors on strain heterogeneities are investigated. Obvious candidates are grain size and grain orientation. Furthermore, as already mentioned, the mean disorientation to neighboring grains has been computed to try to account for the environment of the grains. Consequently, the grain parameters considered in this subsection are the maximum Feret diameter, the tensile modulus (elastic anisotropy), the maximum Schmid factor (onset of plastic activity) and the mean disorientation with regard to neighboring grains. The maximum Schmid factor is computed by taking into account only the {110} and {112} slip systems as justified by the previous slip analysis in subsection 3.2. In addition, 82 grains are excluded ($\approx$ 33 % of the total amount of grains that represent 1 % of the surface of interest) because their area is smaller than 16x16 pixels (one measurement point). Among the remaining 160 grains, the maximum Feret diameter ranges from 82 µm to 2545 µm, the maximum Schmid factor from 0.34 to 0.5, the tensile modulus from 135 GPa to 282 GPa and the mean disorientation to neighbors from 12° to 60°. The grain-averaged von Mises strain after elastic unloading (the choice of the equivalent strain facilitates the analysis, as all strain components are considered) is plotted against these four parameters in Fig. 7a. High dispersion is observed which means that none of them is decisive on its own.

The Spearman rank-order correlation is used to evaluate the relative influence of these parameters on the grain-averaged strain [61]. It investigates the correlation between the ranks of both datasets, i.e. whether a monotonic increase of one dataset is accompanied by a monotonic increase of the other one. The outputs of the Spearman correlation are the Spearman correlation coefficient $\rho$ and the p-value. $\rho$ is distributed between -1 and 1, denoting respectively negative and positive perfect correlation. A correlation coefficient equal to 0 means no correlation. The p-value is distributed between 0 and 1 and assesses the statistical significance of the result, with regard to a null hypothesis $H_0$ and a significance level $\alpha$. Here, $H_0$ is the hypothesis that "the datasets are not correlated" and $\alpha$ is arbitrarily set to 0.01. Simply said, if $p < \alpha$, it is deemed unlikely that two random, i.e. a fortiori uncorrelated, datasets could yield a correlation coefficient $\rho$ greater than the one that has been computed. In that case, $H_0$ can be rejected and $\rho$ can be further analyzed. The Spearman correlation is detailed in the appendix B. The output Spearman correlation coefficients and p-values corresponding to above-mentioned grain parameters are indicated in Fig. 7a. On the one hand, the maximum Feret diameter and the mean disorientation to neighbors produce both high p-values and correlation coefficients close to zero. Therefore, the corresponding statistical results are not significant. The null hypothesis $H_0$ is not rejected and it is concluded that the datasets are not correlated. On the other hand, the maximum Schmid factor and the Tensile modulus, which both characterize the crystallographic orientation of the grains, produce p-values lower than the significance level $\alpha$ and correlation coefficients equal to 0.24 and -0.27 respectively. $H_0$ can be rejected and, based on the values of the computed correlation coefficients, a weak correlation exists. The influence of the maximum Schmid factor is positive, i.e. higher values tend to lead to higher grain-averaged strain, and inversely with regard to the Tensile modulus. In parallel, note that similar correlations have been investigated with the grain-averaged lattice rotation ($\Theta$), but the results are not statistically significant.

Concerning the maximum Schmid factor, this result is well understood considering the Schmid's law: higher values mean that the critical resolved shear stress is lower and slip will

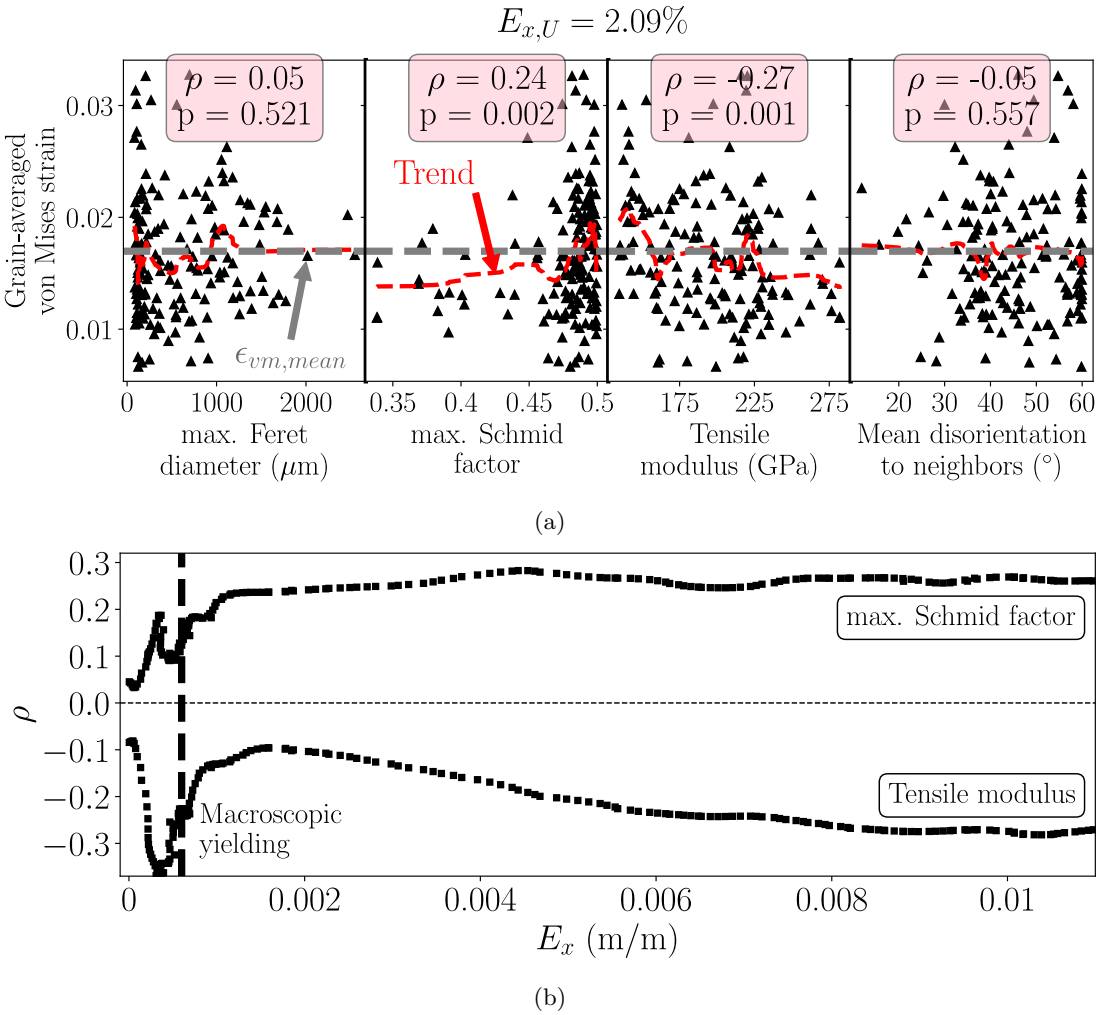


Figure 7: (a) Grain-averaged von Mises strain after elastic unloading ($E_{x,U}$ = 2.09 %) as a function of several grain parameters (from left to right: maximum Feret diameter, maximum Schmid factor, tensile modulus $E_\sigma$ and mean disorientation to neighbors). For each parameter, a Spearman correlation statistical test is performed. $\rho$ and $p$ correspond to output Spearman correlation coefficient and associated p-value respectively. The gray horizontal line corresponds to the mean von Mises strain in the whole region of interest. The red dashed lines have been computed by averaging black triangle markers. They are presented for better visualization.
(b) Evolution of Spearman correlation coefficient $\rho$ between grain-averaged strain and both the maximum Schmid factor and the Tensile modulus, up to $E_x$ = 1 %. For these two parameters, for every image during the test, a Spearman correlation statistical test is performed between grain-averaged von Mises strain and the parameter in question. The remaining two parameters do not show statistical significance and are not considered.

occur earlier. In the literature, such correlation between this parameter and the measured strain has mainly been reported in the case of FCC [35] or hexagonal structures [62]. It is less clear when it comes to BCC crystals [15]. In tantalum, the Spearman correlation coefficient was found

equal to 0.1 in a polycrystal and 0.8 in an oligocrystal [21]. The higher coefficient measured in this work is probably the consequence of the lower number of grain in the surface of interest. In details, most grains in the vicinity of the intergranular strain localizations highlighted in Fig. 4a have high maximum Schmid factors. Besides, the small grain that has forced the deformation to circle around (highlighted in the same figure) shows one of the lowest maximum Schmid factor in the microstructure (0.34). On the contrary, many grains with high maximum Schmid factor record low grain-averaged strain, hence the weak correlation. Besides, in this study, Schmid factors are computed based on external uniaxial stress which definitely differs from the local stress state.

Concerning the Tensile modulus, few studies mention this parameter. It has been shown that the elastic anistropy of the grains affect the subsequent plastic distribution [23, 25, 32]. Yet, it is unclear whether the (weak) correlation should be explained only by elastic anisotropy of the grains, which induces heterogeneous stress before the elastic-plastic transition, or also because grains with low Tensile modulus tend to have high maximum Schmid factor in the presented microstructure, as emphasized in Fig. 2c. A strength-to-stiffness ratio is proposed in the literature [63] but such parameter does not improve the correlation in our investigation.

Regarding the grain size, several justified concerns can be made: i) only a 2D cross-section of the grains is known, which does not necessarily determine the true grain size in the volume, ii) the grains located on the left and right boundaries of the region of interest are cut and iii) the number of activated slip systems and the disorientation have been reported to increase with grain size [12, 19]. However, i) the microstructure should be isotropic [53], ii) the same result is obtained by excluding the cut-off grains from the correlation and iii) both extra slip systems and large disorientation have been observed next to the boundaries in this study, which is more related to the interactions with neighboring grains than to the average deformation in the grain. Furthermore, in the aforementioned Spearman analysis on tantalum, no correlation was found with grain size either [21].

Finally, the fact that the correlation with the latter parameters is weak at best confirms that no single parameter plays a decisive role, and, as a result, that plastic heterogeneities are governed by the influence of grain interactions. In that regard, it is disappointing to see no correlation between grain-averaged strain and the mean disorientation to neighboring grains. Consequently, it suggests that i) disorientation is not an appropriate metric when describing grain environment, as concluded in an aluminum bicrystal [64], ii) longer-range interactions also play an important role, as pointed out in [18], and iii) the grains in the bulk of the specimen are as important as the neighboring grains on the free surface. Regarding the latter, it has indeed been shown by Zeghadi et. al., through crystal plasticity finite element simulations, that underlying grains in the volume have a major impact on the local strain fields measured on the free surface, both in the elastic and plastic regimes [65, 66]. As a consequence, this concern, which cannot be addressed by the present investigation, is expected to affect the correlations with all four parameters.

This investigation has been reproduced for every image during the test in order to strengthen the results. It also allows studying the temporal evolution of the influence of the maximum Schmid factor and the Tensile modulus on the grain-averaged strain. The evolution of the corresponding correlation coefficients $\rho$ is plotted in Fig. 7b up to $E_x = 1\,\%$ for better visualization. The maximum Schmid factor correlation coefficient increases slightly in the elastic domain until $\rho \approx 0.1$, then increases again, at $E_x \approx 0.05\,\%$, shortly before the macroscopic yielding, until it reaches a stabilized value, around $E_x \approx 0.12\,\%$, that corresponds to the one computed at $E_{x,U} = 2.09\,\%$. As for the Tensile modulus correlation coefficient, its absolute value increases in the elastic domain until $|\rho| \approx 0.3$, then decreases until $|\rho| \approx 0.1$ (between $E_x \approx 0.05\,\%$ and $0.16\,\%$), and finally increases back to its stabilized value that is reached around $E_x \approx 0.8\,\%$.

These observations suggest two results. Firstly, during the elastic loading, the increase of the absolute value of the Tensile modulus correlation coefficient is logical since this parameter is meant to characterize the elastic anisotropy of the grains. Because grains with low Tensile modulus tend to have high maximum Schmid factor, the maximum Schmid factor correlation coefficient increases as well. It can be stated that the (weak) correlation between the Tensile modulus and the grain-averaged strain is the result of elastic anisotropy, that induces stress heterogeneities early on.

Secondly, at $E_x \approx 0.05\,\%$, the first plastic heterogeneities are measured, as presented in Fig.3a, hence the important increase of the maximum Schmid factor correlation coefficient from then on. It is interesting to note that its stabilized value is reached quickly, before $E_x = 0.2\,\%$, i.e. before the beginning of the strain accumulation stage, as analyzed in the previous subsection. This indicates that the (weak) influence of the maximum Schmid factor on the grain-averaged strain exists mainly in the "build-up of the plastic deformation pattern". On the contrary, the maximum Schmid factor is not an accurate parameter to understand the strain localizations, apart from the fact that the localizations are found along the initially drawn plastic deformation pattern. This might explain why the maximum Schmid factor is sometimes reported to show no influence on strain heterogeneities, when the strain accumulation stage is not differentiated from the build-up of the plastic deformation pattern. On the opposite, the Schmid law was reported to be statistically satisfied at very low plastic strains [55].

This scale of investigation allows for a hint at how the plastic deformation pattern is built-up around the macroscopic yielding. No correlation has been found between grain-averaged strain and grain size, but a weak correlation has been found with the crystallographic orientation of the grains, as characterized by the Tensile modulus and the maximum Schmid factor. It is deduced that early stress heterogeneities induced by the elastic anisotropy of the grains and the different onsets of slip play a role in the build-up of the plastic deformation pattern. Yet, the weak correlation coefficients support the first-order influence of grain environment, which is unfortunately not captured by the mean disorientation to neighbors, especially given that the underlying microstructure in the volume is not known. Furthermore, this scale brings another confirmation that strain localizations occur in a second time, once the plastic deformation pattern is drawn. However, this approach remains limited. The occurrence of strain localization is not resolved: firstly, abovementioned metrics are related to grains and cannot deal with the behavior of grain boundaries, where strain is often localized. Secondly, the confined scale of plastic localizations is lower than the scale of the grains. For these reasons, a finer investigation is required.

## 3.5 Local investigation of strain heterogeneities and localizations

Understanding the deformation taking place in the specimen calls for in-depth identification of slip systems contributing to the deformation. Manual identification over such a large area is too cumbersome and automatization of the process is uncertain (wavy traces, superposition, variable contrast). An alternative is to identify active slip systems based on their relative contribution to local deformation. It has already been achieved with the "relative displacement ratio" [67], but this metric requires to measure the discontinuities in the displacement field induced by slip events, which is not the case in this study. Therefore, the following paragraphs detail two original methods of slip identification: i) after elastic unloading and ii) during loading. Then, the methods are applied in a magnified region to investigate strain localizations in the presented tensile test.

| 1 | 2 | 3 | 4 | 5 | 6 |
|---|---|---|---|---|---|
| $(110)[1\bar{1}1]$ | $(110)[\bar{1}11]$ | $(1\bar{1}0)[111]$ | $(1\bar{1}0)[11\bar{1}]$ | $(101)[11\bar{1}]$ | $(101)[\bar{1}11]$ |
| 7 | 8 | 9 | 10 | 11 | 12 |
| $(10\bar{1})[111]$ | $(10\bar{1})[1\bar{1}1]$ | $(011)[11\bar{1}]$ | $(011)[1\bar{1}1]$ | $(01\bar{1})[111]$ | $(01\bar{1})[\bar{1}11]$ |
| 13 | 14 | 15 | 16 | 17 | 18 |
| $(112)[11\bar{1}]$ | $(11\bar{2})[111]$ | $(1\bar{1}2)[\bar{1}11]$ | $(\bar{1}12)[1\bar{1}1]$ | $(121)[1\bar{1}1]$ | $(12\bar{1})[\bar{1}11]$ |
| 19 | 20 | 21 | 22 | 23 | 24 |
| $(1\bar{2}1)[111]$ | $(\bar{1}21)[11\bar{1}]$ | $(211)[\bar{1}11]$ | $(21\bar{1})[1\bar{1}1]$ | $(2\bar{1}1)[11\bar{1}]$ | $(\bar{2}11)[111]$ |

Table 2: Notation for the 24 considered slip systems

### 3.5.1 Kinematics identification of slip activity after elastic unloading

The theory of crystal plasticity dictates that slip is activated when the resolved shear stress acting on a slip system reaches a critical value. The resolved shear stress is computed by projecting the local stress state onto the slip plane normal and slip direction. The contribution of the slip system $\alpha$ to the deformation is measured through its slip rate $\dot{\gamma}_\alpha$ which is assumed to be a function of the resolved shear stress. If multiple systems are involved, the plastic velocity gradient tensor $\underline{\underline{L^p}}$ is written to be equal to the sum of the individual contributions of each slip system:

$$\underline{\underline{L^p}} = \sum_\alpha \dot{\gamma}_\alpha (\underline{d_\alpha} \otimes \underline{n_\alpha}) \tag{1}$$

where $\underline{d_\alpha}$ and $\underline{n_\alpha}$ are slip direction and slip plane normal unit vectors respectively. In addition, if plastic deformation is assumed to occur by slip only, above equation can be integrated into:

$$\underline{\underline{H^p}} = \sum_\alpha \gamma_\alpha (\underline{d_\alpha} \otimes \underline{n_\alpha}) \tag{2}$$

where $\underline{\underline{H^p}}$ is the plastic displacement gradient tensor and $\gamma_\alpha$ is the total plastic shear glide. This leads to 9 equations (one for each component of the tensor), but 24 systems are candidates (both $\{110\}$ and $\{112\}$ families are considered, but $\{123\}$ slip systems are not, for simplification; see Tab. 2 for notation). Therefore, if the number of considered slip systems is somehow reduced to 9 or lower, and if the elastic and plastic parts of the displacement gradient tensor can be isolated, slip activity can be accessed. Such kinematics identification has already proven successful when coupled with numerical simulations [30, 68].

The originality of the method presented in this paper is to identify active slip systems based solely on experimental measurements. The starting point is the displacement gradient tensor:

$$\underline{\underline{H}} = \begin{pmatrix} H_x & H_{xy} & H_{xz} \\ H_{yx} & H_y & H_{yz} \\ H_{zx} & H_{zy} & H_z \end{pmatrix}$$

at $E_{x,U} = 2.09\,\%$ (after elastic unloading), whose in-plane components ($H_x$, $H_y$, $H_{xy}$ and $H_{yx}$) are measured with DIC, as illustrated in Fig. 8a. Firstly, the following assumptions are made:

- Elastic contribution is neglected: $\underline{\underline{H^p}} \approx \underline{\underline{H}}$.

- By plastic incompressibility, $\mathrm{tr}(\underline{\underline{H}}) = 0 \rightarrow H_z = -(H_x + H_y)$.
- The remaining components are not known and are supposed equal to zero: $H_{zx} = H_{zy} = H_{xz} = H_{yz} = 0$

The first and second assumptions are commonly found in slip identification strategies [30, 68]. The first one is all the more justified by the elastic unloading. The third assumption is subject to errors, especially as non-negligible out-of-plane motion occurred during the test, as pointed out in subsection 3.2.

Secondly, the resulting displacement gradient tensor can be projected onto every candidate slip system:

$$H_\alpha = \underline{n_\alpha} \cdot \underline{\underline{H}} \cdot \underline{d_\alpha} \tag{3}$$

A (non zero) scalar value is obtained for every system and for every measurement point, as shown in Fig. 8b. However, only a few slip systems do work locally as supported by the investigation of slip marks in this work and in the literature [44]. Therefore it is emphasized that this projected displacement gradient scalar is *not* the shear glide $\gamma_\alpha$ from Eq. 2. It should rather be regarded as the likelihood that the corresponding slip system has contributed to deformation.

Finally, in order to obtain $\gamma_\alpha$, the number of considered slip systems must be reduced to 9 or less, as said previously. Thanks to the previous step, the 24 values of $H_\alpha$ establish an objective criterion to discriminate the slip systems: the systems to consider are the ones that correspond to the nine greatest $|H_\alpha|$. Nevertheless, with the presented results, solving Eq. 2 with more than two slip systems sometimes leads to absurd values. Therefore only the two systems with the greatest $|H_\alpha|$ are considered. A flowchart is provided as a supplementary material (supplementary_material_flowchart.pdf). The presented kinematics identification is illustrated in Fig. 8c. The results exhibit the systems 2, 4, 18, 21 and 23 as active. Minor activity of the systems 6 is also measured, but it could be an artifact. An arbitrarily threshold level can be set to distinguish active systems from noise. In practice, all $\gamma_\alpha$ values are summed over in the entire grain, for every slip system, and the threshold level is equal to 10 % of the largest summation, i.e. with regard to the "most active" system.

The theoretical slip marks corresponding to the kinematically identified slip systems are displayed in Fig. 9b over a magnified area of the region of interest. They are compared to the observed slip marks from the optical micrograph in Fig. 9a. Overall a good agreement is acknowledged. In most grains, the orientation, as well as the spatial distribution and intensity of kinematics slip marks, match the optical micrograph. However, differences are also observed in many areas. It suggests that active slip systems are not always properly identified. Potential sources of error are i) EBSD and DIC measurement uncertainty, ii) local elastic contribution, iii) unknown out-of-plane displacement gradient components, iv) occurrence of {123} slip (or any other slip than on the well-defined 24 systems) and v) more than two systems being active in a same measurement point. The major source of error is probably the unknown out-of-plane components in $\underline{\underline{H}}$, which form 5 out of 9 components in total. Besides, a non-negligible out-of-plane motion has been pointed out in subsection 3.2. Nevertheless, the presented method allows a satisfying identification of active slip systems all over the surface of interest. In addition, corresponding shear glide values are obtained.

### 3.5.2 Kinematics identification of slip activity during loading

Unfortunately, the previous analysis is restricted to the elastic unloading, at the end of the test ($E_{x,U} = 2.09\,\%$), once the elastic contribution can be neglected. The displacement gradient tensor $\underline{\underline{H}}$ is not relevant in the elastic-plastic transition. Instead, in order to investigate slip activity

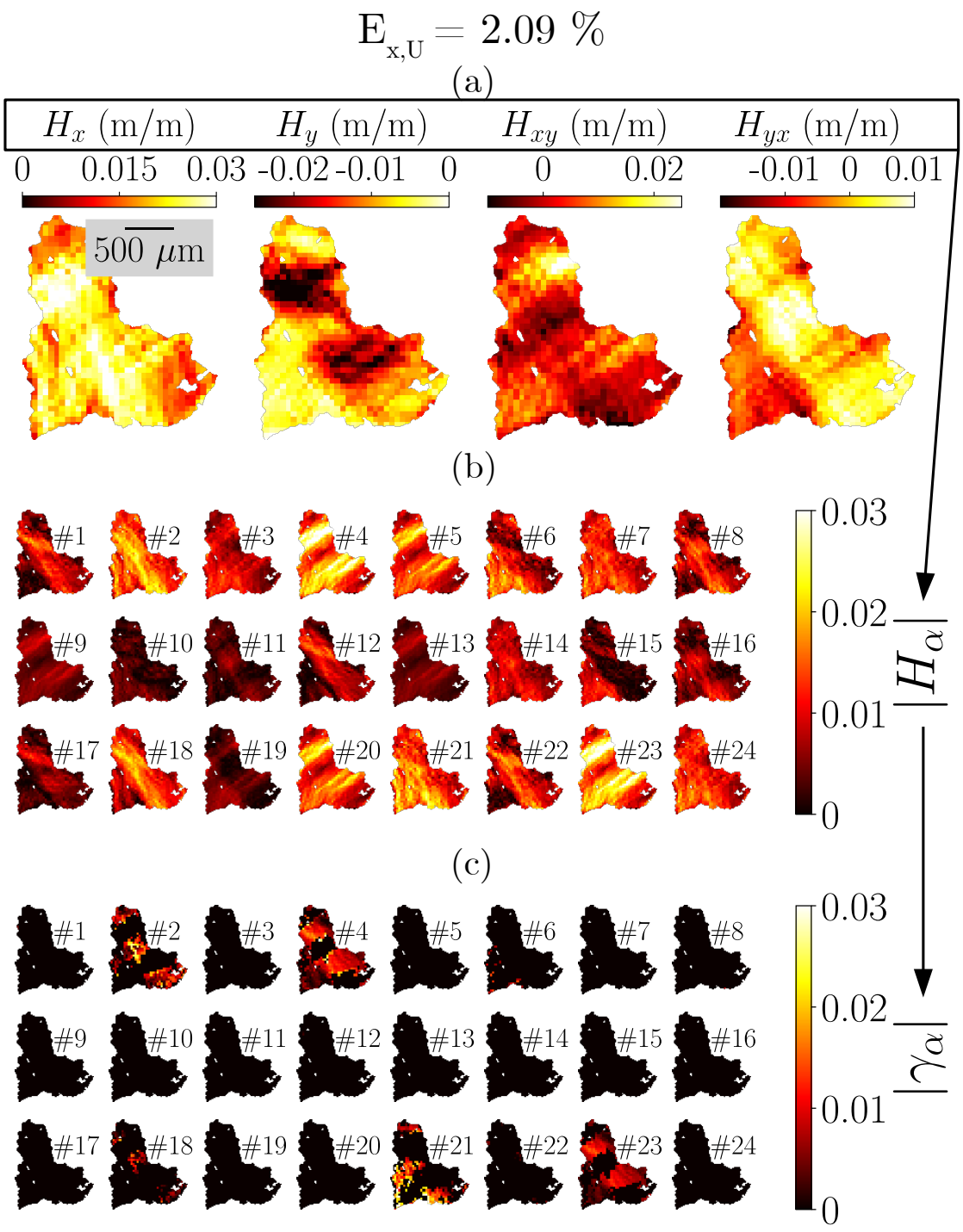


Figure 8: Illustration of kinematics identification of slip activity at $E_{x,U} = 2.09\,\%$ in a given grain: (a) In-plane components of displacement gradient tensor $\underline{\underline{H}}$ measured with Digital Image Correlation. (b) Projected displacement gradient $H_\alpha$ for every slip system $\alpha$ (see Tab. 2). (c) Plastic shear by slip $\gamma_\alpha$ that allows for identification of active slip systems. It is computed after projected displacement gradient $H_\alpha$.

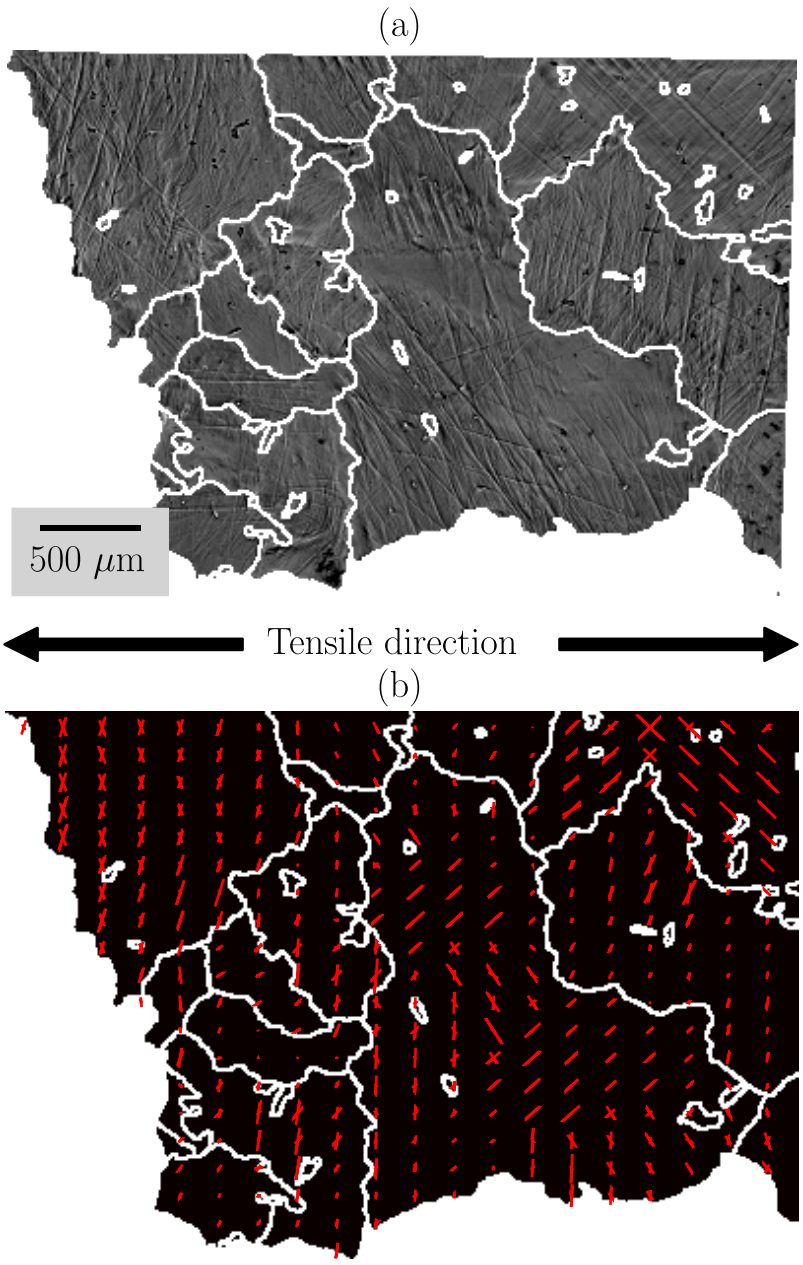


Figure 9: Comparison between (a) slip marks observed on the optical micrograph after the test (b) slip marks corresponding to kinematically identified slip systems, in a magnified area of the region of interest. The length of the latter (red lines) is proportional to the plastic shear by slip of the corresponding system $|\gamma_\alpha|$: the more intense the plastic shear by slip, the longer the line. Contrast of the optical micrograph has been slightly enhanced for better visualization.

around the macroscopic yielding, the velocity gradient tensor $\underline{\underline{L}}$ is considered. Its four in-plane components $L_x$, $L_y$, $L_{xy}$ and $L_{yx}$ are computed by derivating the corresponding components of $\underline{\underline{H}}$ with respect to time. Similarly to the previous method, the remaining out-of-plane components are supposed equal to zero ($L_{zx}$, $L_{zy}$, $L_{xz}$ et $L_{yz}$) or deduced by plastic incompressibility ($L_z$). Obviously, the plastic incompressibility assumption is absurd when the specimen is subjected to elastic deformation. However, elastic velocity gradient is one order of magnitude below slip velocity gradient in the investigated material. As a consequence, the onset of slip is clearly visible. Similarly to the displacement gradient tensor, $\underline{\underline{L}}$ is projected onto every candidate slip system:

$$L_\alpha = \underline{n_\alpha} \cdot \underline{\underline{L}} \cdot \underline{d_\alpha} \tag{4}$$

Contrary to the previous method, the measurements are too noisy to solve back Eq. 1, even when considering only two slip systems. Therefore, it is decided to stick with $L_\alpha$ values. As a result, a scalar value is obtained not only for every system and for every measurement point, but also for every image during the test. In order to process such multi-dimensional data, it is chosen to plot the evolution of slip activity with Hue Saturation Lightness (HSL) representation. For a given measurement point, at a given time, the slip system with maximum $|L_\alpha|$ is displayed. Slip systems are differentiated thanks to the hue channel and corresponding slip rate values are indicated by the lightness channel (bright pixels correspond to low values).

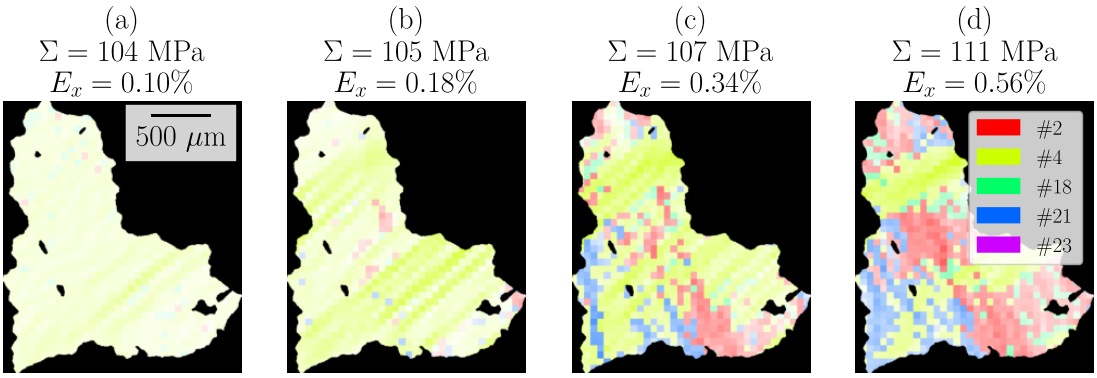


Figure 10: Illustration of kinematics identification of slip activity during loading in a given grain. Slip activity is displayed using Hue Saturation Lightness (HSL) representation: hue indicates the number of the active slip system (from 1 to 24) and lightness indicates the magnitude of the projected velocity gradient on the active slip system $|L_\alpha|$ (brighter pixels correspond to lower values); the saturation channel is not used.
(a) and (b) Onset of plasticity in the grain: only one system is activated with low corresponding activity. (c) and (d) Simultaneous activation of multiple slip systems with increasing loading.

An example of such representation is detailed in Fig. 10. The focus is given to the same grain displayed in Fig. 8, where slip systems 2, 4, 18, 21 and 23 were identified as active based on the measured displacement gradient tensor at $E_{x,U} = 2.09\,\%$. During the macroscopic elastic domain, many systems are displayed randomly as very bright pixels, i.e. with very low $|L_\alpha|$ (not shown here). This corresponds to the absence of plastic activity. After macroscopic yielding, from $E_x \approx 0.1\,\%$, system 4 is activated in the whole grain, first with low values then through more intense bands at approximately 45°, as illustrated in Fig. 10a and 10b. It is only later that other systems are activated: system 2 is observed through an inclined band in the middle

of the grain and system 21 emerges in the lower left of the grain (Fig. 10c). With increasing deformation, these two systems take over previously activated system 4 except for a couple of areas (Fig. 10d). Compared to the kinematics identification after elastic unloading, system 23 is not observed. Since $\gamma_{23}$ shares the same pattern with $\gamma_4$ in Fig. 8c, it is believed that system 23 is outvalued by system 4 during the entire loading in Fig. 10. The slip marks, visible on the optical micrograph in Fig. 9a, cannot invalidate this assumption because the theoretical angles between the tensile direction and the corresponding slip marks are both equal to 42°. Furthermore, the fact that system 4 has been taken over early explains why its corresponding slip marks at 42° are hardly observed in the optical micrograph in Fig. 9a. In addition, system 18 is only observed sparsely around system 2 in Fig. 10, which suggests that it was wrongfully identified earlier. In this case, it is confirmed by the optical micrograph where no corresponding slip mark is seen on the surface.

It is acknowledged that for better visualization, only the five systems that were identified in Fig. 8 were fed to Fig. 10. Indeed, it is impossible to differentiate 24 slip systems in the same time by using the HSL representation. Yet, no other activity than the previously mentioned slip systems is seen in this grain. Therefore, the presented method brings valuable information to the kinematics identification performed after elastic unloading. Used jointly, slip systems can be identified with more confidence and, last but not least, slip activity during the elastic-plastic transition can be investigated. In return, $L_\alpha$ values are more prone to noise.

### 3.5.3 Application to a magnified region

A magnified area that features 33 grains is presented in Fig. 11a with the corresponding grain labels. This area exhibits many intense strain localizations, as seen on the local von Mises strain at $\underset{\sim}{E}x, U = 2.09\,\%$ in Fig. 11b. The magnitude of the gradient of out-of-plane displacement $||\vec{\nabla Z}||$ and the Grain Initial Orientation Deviation $\Theta$, both computed from the characterization of the deformed surface as explained in subsection 3.2, are displayed in Fig. 11c and 11d respectively. The observations from the previous sections are repeated: i) strain is mostly localized around some grain boundaries (179-150, 145-150, 176-170 and 170-168). In most cases, the localizations seem to be contained in one side of the boundary. ii) Significant out-of-plane motion occurred during the test, but $||\vec{\nabla Z}||$ is much more localized than $\epsilon_{vm}$: boundaries 179-150 and 176-170 record high in-plane strain but moderate out-of-plane activity. However, it seems that all out-of-plane localizations are observed in areas corresponding to high in-plane strain. iii) $\Theta$ is particularly heterogeneous. High lattice rotation is measured in grain 170 and on the right side of boundaries 179-150 and 145-150. Furthermore, subdivision of the grain 179 has started to occur, as shown by an inclined band of low values at 45°.

In order to complete these observations, the previous slip identification methods are applied in the corresponding magnified area. Firstly, the active slip systems identified after elastic unloading are displayed in Fig. 12. They are superposed on the slip marks actually observed on the optical micrograph of the deformed surface. In case of good correspondence, the system index as well as its corresponding mark on the deformed surface are reported in green solid lines. If the identified system does not match any mark, it is reported in orange with its theoretical slip mark as a dashed line. Remaining slip marks, that correspond to slip systems that were not identified with the method, are manually identified (following the methodology explained in section 3.2) and reported in pink solid lines. The results show that most systems are correctly identified. In this magnified area, the major mistakes can be explained by more than two systems activated in the same measurement point, such as in the grain 179 where systems 3, 6, 8 and 15 show superposed marks, or by slip on {123} plane such as in grain 145.

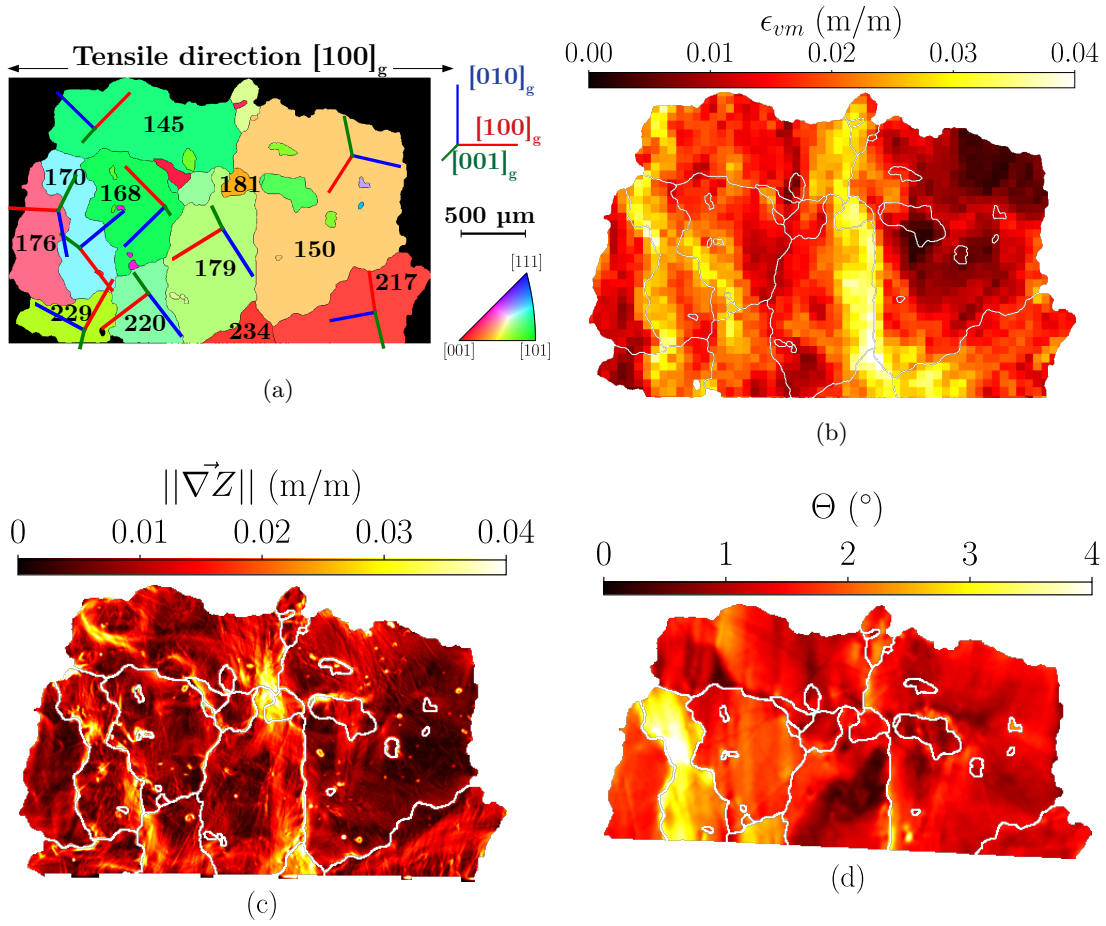


Figure 11: (a) Inverse Pole Figure mapping (with regard to the tensile direction) of a magnified area that exhibits intense strain localizations. Corresponding grain labels and coordinate systems are indicated. (b) von Mises strain $\epsilon_{vm}$ at $E_{x,U} = 2.09\,\%$ in the corresponding area. (c) Magnitude of the gradient of out-of-plane displacement $||\vec{\nabla}Z||$ in the corresponding area, computed from profilometry measurements of the deformed surface. (d) Grain Initial Orientation Deviation $\Theta$ in the corresponding area, computed from the crystallographic orientation of the deformed surface (incomplete, in particular the bottom part is missing).

Consequently, the slip systems identified after elastic unloading are fed to the HSL representation of slip activity during the elastic-plastic transition, similarly to the previous demonstration. It is acknowledged that only the systems that contribute the most to the measured strain localizations in the magnified area are displayed, so that the systems can be differentiated without altering the measured kinematics. The results are presented in Fig. 13; they are accompanied by the corresponding strain fields $\epsilon_{vm}$. They are also provided as an animation in the online version (supplementary_material_video_B.mp4). At $E_x = 0.05\,\%$ (Fig. 13a), before macroscopic yielding, a first strain localization is measured near the boundary 179-150, as already highlighted in Fig. 3a. It corresponds to the activation of the system 15 in the grain 179. No other plastic activity is observed in the magnified area. At $E_x = 0.06\,\%$ (Fig. 13b), corresponding to the on-

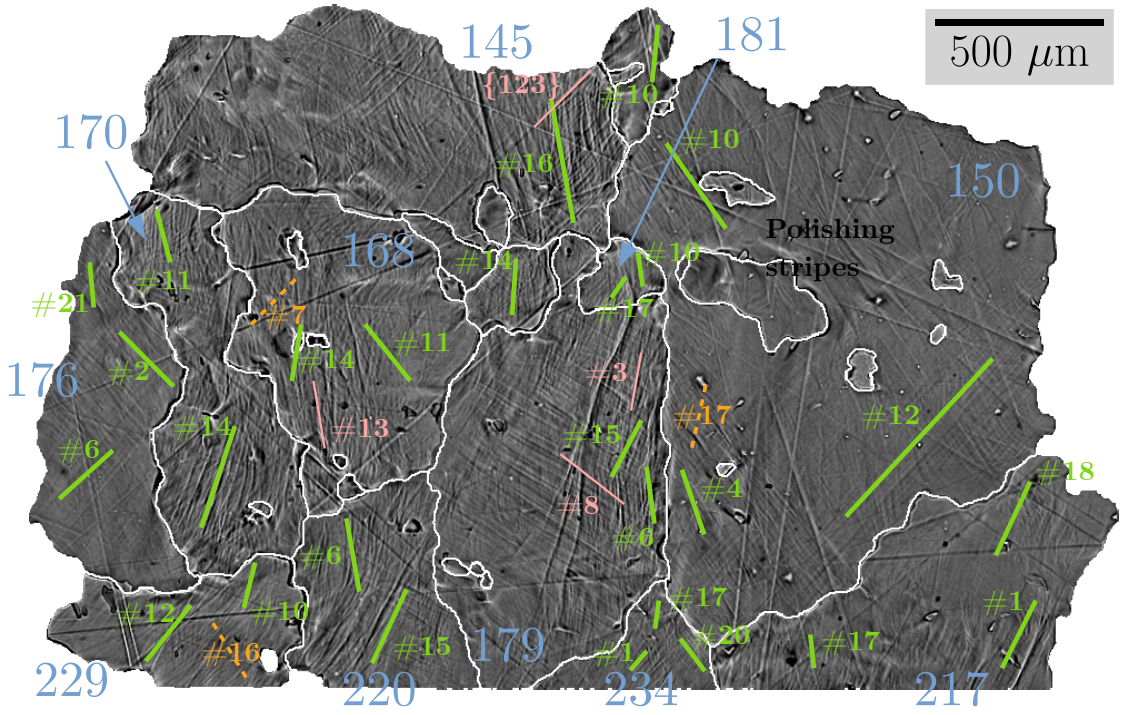


Figure 12: Slip marks in the magnified area that are observed on the optical micrograph. The corresponding slip systems are compared to the systems identified after the elastic unloading. The notation is the following: green solid lines for slip marks that belong to kinematically identified systems), orange dashed lines for kinematically identified systems whose corresponding marks are not observed on the micrograph and pink solid lines for remaining slip marks matching a system which has not been kinematically identified. Some grain labels are reminded in light blue.

set of macroscopic yielding, plastic activity of boundary 179-150 has extended to the left in the interior of the grain 179 and upwards through grain 181 (system 17), up to the boundary 145-150 (slip most likely occurs on {123} plane, hence no plastic activity is seen on the corresponding HSL representation). In parallel, slip occurs around the triple junction 176-170-229, on system 6 (grain 176), 14 (grain 170) and 10 (grain 229). At $E_x = 0.08\,\%$ (Fig. 13c), system 6 emerges in grain 179 and progressively takes over previously activated system 15 (Fig. 13d corresponding to $E_x = 0.15\,\%$). It triggers the activation of several slip systems in the nearby grains: system 17 in the grains 150 (other side of the boundary) and 234 (downwards), system 10 in the grain 181 and system 16 in the grain 145 (upwards). In parallel, new slip systems have also emerged around the triple junction 176-170-229 (Fig. 13c, activation of system 2 in grain 176, 11 in grain 170 and 16 in grain 229). Similarly, the consequent slip dynamics in grains 168 and 220 is modified (Fig. 13d). Finally, between $E_x = 0.15\,\%$ and $E_x = 0.22\,\%$ (Fig. 13e), the active slip systems have barely changed and strain values have increased significantly around boundaries 179-150, 176-170, 170-168 and triple junctions 179-150-234, 176-170-229 and 229-220-170. These localizations seem to correspond to areas where a high number of slip systems are activated at the same time, in a reduced area.

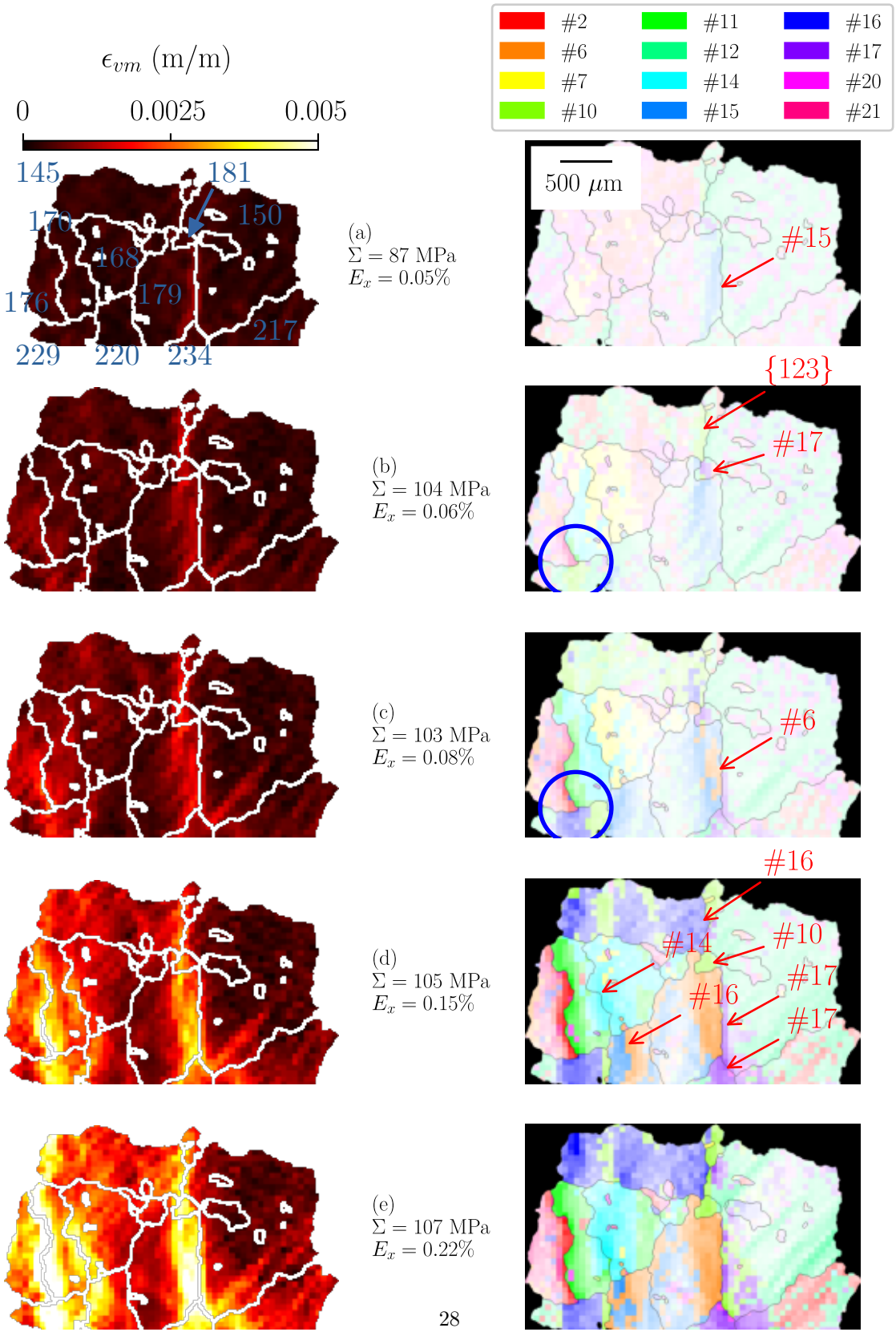




Figure 13: Evolution of von Mises equivalent strain $\epsilon_{vm}$ and slip activity (kinematics identification during loading) in the magnified area during the elastic-plastic transition. (a) Before macroscopic yielding, (b) onset of macroscopic yielding, (c), (d) and (e) plastic domain. Red arrows and circular patches highlight activated slip systems that are detailed in the text.

These observations suggest that the build-up of the plastic deformation pattern results from the spreading of slip and the following dynamics of slip systems interacting one with another. The first slip systems to activate will spread until nearby boundaries where they are likely to trigger the activation of other systems, as described in [28] in an austenitic stainless steel. This is even more observed around triple junctions, similarly to bulk measurements in a nickel-based superalloy [27]. With new systems emerging and interacting, the local stress state is modified, which could explain why previous slip systems are sometimes replaced by recently activated ones. After a certain amount of time, the current kinematics stabilizes and deformation is carried by the remaining active slip systems. Lattice rotation and out-of-plane motion (in the free surfaces) can help in reaching this equilibrium, as illustrated in grain 170 in Fig. 11c and 11d. Finally, strain will accumulate where the higher amount of slip systems is found. This corresponds mostly to triple junctions and grain boundaries, as pointed out in subsection 3.2, where it has been shown that internal stresses are the highest [13, 14] and more systems are required to accommodate the deformation [26, 69].

These analyses prove that the strain heterogeneities measured at the end of the test depend partly on the first slip systems to activate, since they affect the subsequent kinematics. This explains the (weak) influence of the maximum Schmid factor on the grain-averaged strain thas was measured in the subsection 3.4. In addition, the role of the grain environment on the strain heterogeneities is shown. Indeed, the kinematics in a given grain partly depends on the slip systems coming from nearby grains and acting on all the boundaries. For instance, Musinski et. al. have measured the transfer of the resolved shear stresses from grains that exhibit higher plasticity to surrounding lower plastic activity grains [32]. These interactions between grains cannot be captured by the mean disorientation to neighboring grains, nor probably by any other granular parameter. They are added to the stresses induced beforehand by the elastic anisotropy of the crystals, in the elastic regime, as suggested by the (weak) correlation between the grain-averaged strain and the tensile modulus. Also, it should be recalled that all these interactions take place not only with the neighboring grains in the surface, but also with those (unknown) in the volume.

Therefore, local investigation with the presented strategy of identification of slip activity fills in part the limitations of global and grain-scale analyses. Computations are no longer performed based on external quantities but on local kinematics, and interactions between active slip systems and grain boundaries can be analyzed. The build-up of the plastic deformation pattern is better understood and the occurrence of plastic localizations, where strain accumulates with increasing loading, is investigated. In particular, they seem to arise from simultaneous activity of several slip systems, which tends to happen in the vicinity of grain boundaries and triple junctions. Yet, a strong assumption in this work is that slip systems are considered as being independent from one another. However, the dynamics of slip is obviously affected by the interactions between dislocations [70], which can, for instance, repel each other. Similarly, the behavior of dislocations when encountering grain boundaries is an active field of research [71, 72]. For example, Patriarca et. al. have shown that the strain profile across grain boundaries depends on the transmission or absorption of dislocation by the grain boundaries [73]. In another experimental investigation, the resolved shear stress acting on the boundary was highlighted [33]. Such quantity can be obtained by solving equilibrium equations to obtain the local stress state. This is an obvious prospect of this work, especially as the free-surfaces of the specimen are preserved in this test. This should improve the experimental-numerical dialogue.

# 4 Conclusions and prospects

In this paper, full-field kinematics measurements have been performed on the surface of a polycrystalline coarse-grained $\alpha$-Fe specimen subjected to monotonic tension up to approximately 2 % deformation followed by elastic unloading. Special care was given to the optical-based DIC measurement chain (choice of optical device, fabrication of speckle pattern) in order to obtain accurate measurements at the microstructural scale (spatial resolution equal to 55 µm) with high temporal resolution (one image acquired every $7 \times 10^{-5}$ strain increment). Thanks to the careful repositioning of crystallographic orientation of the microstructure obtained by EBSD scan of the surface prior to the test, strain fields were analyzed with regard to the microstructure. The results were compared to the characterization of the deformed surface by optical microscopy, profilometry and EBSD. Then, they were discussed through a downscaling strategy from global to grain-scale and finally local analyses. The latter was performed after projection of displacement gradient fields after elastic unloading and velocity gradient fields during the test onto BCC slip systems. This original approach allowed investigation of slip activity based solely on the experimental measurements. The main results are:

- Upon yielding, strain heterogeneities develop at a scale larger than the grain's, draw a steady plastic deformation pattern and, in a second stage, result in strain localizations that occur mostly around grain boundaries and triple junctions. Because of the differences in scale and occurrence, strain localizations are differentiated from the coarse steady.
- No correlation is found between grain-averaged strain and grain size, but a weak correlation is found with grain orientation. It is suggested that elastic anisotropy and varying onsets of slip influence the build-up of the steady plastic deformation pattern. Yet, the weak correlation also highlights the major influence of grain environment, which is not captured by the mean disorientation to neighboring grains. In fact, the local analysis revealed that no grain-scale metrics is likely to characterize the effect of the environment of a given grain since it partly depends on local interactions between its boundaries and the activated slip systems in neighboring grains.
- Strain localizations seem to result from simultaneous activity of several slip systems in a reduced area, which is more likely to occur in the vicinity of grain boundaries and triple junctions.

Yet, even our local scale of investigation cannot address the scale of dislocations. Besides, as in every surface investigation, the unknown underlying microstructure in the volume affects the measured kinematics fields on the free surface. In parallel, the representativity of surface measurements with regard to the behavior in the volume is uncertain. Nevertheless, optical-based DIC has proven to be a suitable tool for analyzing strain heterogeneities and localizations at the scale of the microstructure of a metallic polycrystal. In order to characterize fine and complex industrial microstructure, the main challenge is to further improve the spatial resolution while maintaining high measurement accuracy. In that regard, a possibility of improvement is to perform a full-field measurement method with two cameras mounted on a stereo-microscope. It would allow to measure local out-of-plane motion during the test and strengthen the kinematics identification of slip activity. Last but not least, dialogue with numerical simulations is an obvious prospect as it is required for investigation of the local stress state. Comparison with numerical results is expected to be fruitful as specimen free-surfaces were preserved in this study. Such investigation requires preliminary work [74] and will be the scope of an upcoming paper.

**Acknowledgements** This work has been carried out within the CNRS SWIT'lab joint laboratory (MG-Valdunes, LaMcube, Université de Lille, École Centrale de Lille, LAMIH, Université Polytechnique des Hauts de France, CNRS) and has also been supported by the ELSAT2020 research project. SWIT'lab and ELSAT2020 are co-financed by the European Union with the European Regional Development Fund, the French state and the Hauts de France Region Council.

# Appendix A: crystallographic computations

Rotation from the (global) specimen coordinate system to the (local) crystal coordinate system can be described with the following rotation matrix:

$$R = \begin{pmatrix} C_2C_1 - S_2CS_1 & C_2S_1 + S_2CC_1 & S_2S \\ -C_2CS_1 - S_2C_1 & C_2CC_1 - S_2S_1 & C_2S \\ SS_1 & -SC_1 & C \end{pmatrix}$$

where $C$ and $S$ abbreviate the cosine and sine functions and the indices (1, no index, 2) denote the Euler angles ($\phi_1$, $\Phi$, $\phi_2$) in Bunge convention respectively. For example, $S_2CS_1$ corresponds to $\sin\phi_2 \times \cos\Phi \times \sin\phi_1$. Inversely, $R^{-1} = R^T$ is the rotation matrix from local to global coordinate system. As a consequence, a unique rotation matrix is associated to each grain. All further computations are derived:

- Assuming uniaxial stress, the Schmid factor for a given slip system $\alpha$ with slip plane normal unit vector $n_\alpha$ and slip direction unit vector $d_\alpha$ is equal to $\mu = (n_\alpha \cdot R\sigma) \times (d_\alpha \cdot R\sigma)$ where $\sigma$ is the load direction unit vector in global specimen coordinates ($R\sigma$ becomes the load direction unit vector in local crystal coordinates).
- The angle $\Pi$ between surface marks caused by slip system $\alpha$ and the loading direction agrees with $\cos\Pi = (n_\alpha \times Rz) \cdot R\sigma$ where $z$ is the surface plane unit vector [75]. In practice $\sin\Pi$, which is equal to the determinant of the 2x2 matrix formed by the in-plane components of $(n_\alpha \times Rz)$ and $R\sigma$, is also computed in order to return values between $-90°$ and $90°$.
- The tensile modulus is equal to $E_\sigma = \frac{1}{S_{11} - 2(S_{11} - S_{12} - \frac{1}{2}S_{44})(\alpha^2\beta^2 + \alpha^2\gamma^2 + \gamma^2\beta^2)}$ where $S_{11}, S_{12}, S_{44}$ are the elastic compliance coefficients of the material and $\alpha, \beta, \gamma$ are the direction cosines between $R\sigma$ and the crystal coordinate system [76]. The compliance coefficients can be derived from stiffness coefficients $C_{11}, C_{12}, C_{44}$, which are found in the literature for the studied material [77]. In details, $S_{11} = \frac{C_{11}+C_{12}}{(C_{11}-C_{12})(C_{11}+2C_{12})}$, $S_{12} = \frac{-C_{12}}{(C_{11}-C_{12})(C_{11}+2C_{12})}$ and $S_{44} = \frac{1}{C_{44}}$.

**Misorientation and disorientation**

The misorientation between two grains is also expressed in terms of rotation matrices. Let $R_A$ and $R_B$ be the orientation matrices of grains A and B; the misorientation matrix from A to B equals to $R_{A/B} = R_B {R_A}^T$. It expresses the successive transformations from coordinate system A to global coordinate system and then from global to B. The *misorientation* angle is then derived with

$$\theta = \arccos\left(\frac{\mathrm{tr}(R_{A/B}) - 1}{2}\right)$$

However, this computation does not take into account the physical symmetries of cubic structures. The actual *disorientation* angle, i.e. the smallest misorientation angle accounting all symmetries, is computed after

$$\theta_{A/B} = \min_{i,j} \arccos\left(\frac{\mathrm{tr}(O_i R_{A/B} O_j) - 1}{2}\right)$$

where $O_{k,1\leq k\leq 24}$ are symmetry operators of cubic structure. The resulting disorientation angle ranges from 0 to 62.8°.

The Grain Initial Orientation Deviation $\Theta$, mentioned in subsection 3.2, is the disorientation angle corresponding to the initial and deformed rotation matrices of a given pixel. It presumes the deformed surface to be repositioned in the reference framework. Furthermore, the mean disorientation to neighbors, mentioned in subsection 3.3, is computed after weighting grain boundaries disorientation values with their corresponding length in the surface seen by the camera.

# Appendix B: Spearman correlation

The Spearman rank-order correlation aims to assess the correlation between two datasets [61]. It is related to the more famous Pearson correlation, but the main difference is that it does *not* seek a linear relationship between the datasets. Rather, it evaluates the relationship between their ranks, i.e. whether a monotonic increase of one dataset is accompanied by a monotonic increase of the other one, regardless of their values. The main output of the Spearman rank-order correlation is the Spearman correlation coefficient $\rho$, which is computed as follows:

$$\rho = \frac{\mathrm{cov}(R(X), R(Y))}{\sigma_{R(X)}\sigma_{R(Y)}}$$

In the above equation, $X$ and $Y$ are the two datasets that are evaluated. $R(x)$ and $R(Y)$ are the ranks of $X$ and $Y$, $\mathrm{cov}(R(X), R(Y))$ is the covariance of the ranks and $\sigma_{R(X)}$ and $\sigma_{R(Y)}$ are the standard deviations of the ranks. This formula is the same that is used in Pearson correlation, but applied to the ranks of the datasets. In other words, the Spearman correlation coefficient is equal to the Pearson correlation coefficient of the ranks of the datasets.

$\rho$ is distributed between -1 and 1. If $\rho = 1$ (resp. -1), there exists a perfect positive (resp. negative) correlation between the ranks of the datasets $X$ and $Y$, i.e. an increase of $X$ is always followed by an increase (resp. decrease) of $Y$. If $\rho = 0$, there is no correlation.

Depending on the dataset, for example if the sample size is small, there exists a risk that the Spearman correlation coefficient is not significant. Therefore, the correlation coefficient is accompanied by the evaluation of the significance of the result. The first step is to define the null hypothesis $H_0$, which is usually the opposite statement of what is investigated. In our application, the aim is to find any potential correlation (negative or positive) between the datasets. Therefore, $H_0$ is: "the two datasets are not correlated". With regard to that hypothesis, the significance of the correlation is the probability that two random, a fortiori uncorrelated, datasets lead to a correlation coefficient $\rho$ greater in absolute value than the one that has been computed previously. This probability is the p-value and is computed in two steps. Firstly, the "t-statistic" is computed:

$$t = \rho\sqrt{\frac{n-2}{1-\rho^2}}$$

where $n$ is the sample size and $\rho$ is the computed Spearman correlation coefficient. Then, the p-value is computed from the value of $t$ with regard to a Student's t-distribution. The latter

depends on $H_0$: in our application, a two-sided distribution is used because both positive and negative correlation are investigated. Therefore, the p-value is equal to:

$$p = 2 * (1 - \text{cdf}(t))$$

where $\text{cdf}(t)$ is the cumulative distribution function of the two-sided t-distribution.

Since it is a probability, $p$ is distributed between 0 and 1. To ultimately decide whether the correlation coefficient is significant, its value should be compared to a significance level $\alpha$ that is fixed arbitrarily. On the one hand, if $p > \alpha$, then it is concluded that the probability that two random datasets lead to a correlation coefficient greater than $\rho$ is too high, and therefore the null hypothesis $H_0$ cannot be rejected: it is likely that the two datasets are not correlated, i.e. the result is not statistically significant. On the other hand, if $p < \alpha$, then the probability that two random datasets lead to a correlation coefficient greater than $\rho$ is low enough to reject $H_0$: the result is deemed statistically significant, and the value of $\rho$ can be further analyzed. As a consequence, the ultimate decision depends on the significance level $\alpha$ that is set. As always in statistics, it is possible to make a mistake by wrongfully rejecting (or not rejecting) the null hypothesis no matter the p-value.

# References


[1] F. Barbe, S. Forest, and G. Cailletaud. "Intergranular and Intragranular Behavior of Polycrystalline Aggregates.Part 2: Results". In: *International Journal of Plasticity* 17.4 (Jan. 2001), pp. 537–563. ISSN: 0749-6419. DOI: 10.1016/S0749-6419(00)00062-0.

[2] C. C. Tasan, J. P. M. Hoefnagels, M. Diehl, D. Yan, F. Roters, and D. Raabe. "Strain Localization and Damage in Dual Phase Steels Investigated by Coupled In-Situ Deformation Experiments and Crystal Plasticity Simulations". In: *International Journal of Plasticity*. Deformation Tensors in Material Modeling in Honor of Prof. Otto T. Bruhns 63 (Dec. 2014), pp. 198–210. ISSN: 0749-6419. DOI: 10.1016/j.ijplas.2014.06.004.

[3] S. Mukherjee, A. Kundu, P. S. De, J. K. Mahato, P. C. Chakraborti, M. Shome, and D. Bhattacharjee. "Insitu Investigation of Tensile Deformation Behaviour of Cold-Rolled Interstitial-Free High-Strength Steel in Scanning Electron Microscope". In: *Materials Science and Engineering: A* 776 (Mar. 2020), p. 139029. ISSN: 0921-5093. DOI: 10.1016/j.msea.2020.139029.

[4] D. Chandrasekaran and M. Nygårds. "A Study of the Surface Deformation Behaviour at Grain Boundaries in an Ultra-Low-Carbon Steel". In: *Acta Materialia* 51.18 (Oct. 2003), pp. 5375–5384. ISSN: 1359-6454. DOI: 10.1016/S1359-6454(03)00394-X.

[5] J. Q. da Fonseca, P. M. Mummery, and P. J. Withers. "Full-Field Strain Mapping by Optical Correlation of Micrographs Acquired during Deformation". In: *Journal of Microscopy* 218.1 (2005), pp. 9–21. ISSN: 1365-2818. DOI: 10.1111/j.1365-2818.2005.01461.x.

[6] M. Henning and H. Vehoff. "Local Mechanical Behavior and Slip Band Formation within Grains of Thin Sheets". In: *Acta Materialia* 53.5 (Mar. 2005), pp. 1285–1292. ISSN: 1359-6454. DOI: 10.1016/j.actamat.2004.10.052.

[7] S. Banerjee, T. Dasgupta, S. Mukherjee, M. Shome, P. C. Chakraborti, and S. K. Saha. "Digital Image Correlation for Grain Scale Strain Measurement in Interstitial Free High Strength Steel". In: *Materials Science and Technology* 32.4 (Mar. 2016), pp. 328–337. ISSN: 0267-0836. DOI: 10.1179/1743284715Y.0000000075.

[8] H. Qiu, R. Ueji, Y. Kimura, and T. Inoue. "Heterogeneous Distribution of Microstrain Evolved During Tensile Deformation of Polycrystalline Plain Low Carbon Steel". In: *Metals* 10.6 (June 2020), p. 774. DOI: 10.3390/met10060774.

[9] Y Tomota, P Lukas, S Harjo, J-H Park, N Tsuchida, and D Neov. "In Situ Neutron Diffraction Study of IF and Ultra Low Carbon Steels upon Tensile Deformation". In: *Acta Materialia* 51.3 (Feb. 2003), pp. 819–830. ISSN: 1359-6454. DOI: 10.1016/S1359-6454(02)00473-1.

[10] T. Hama, T. Nishi, M. Oka, T. Matsuno, Y. Okitsu, S. Hayashi, K. Takada, and H. Takuda. "Non-Uniform Deformation Behavior of Coarse-grained Ultralow Carbon Steel Measured Using Digital Image Correlation Method". In: *ISIJ International* 61.6 (2021), pp. 1971–1979. DOI: 10.2355/isijinternational.ISIJINT-2020-712.

[11] P. Erieau and C. Rey. "Modeling of Deformation and Rotation Bands and of Deformation Induced Grain Boundaries in IF Steel Aggregate during Large Plane Strain Compression". In: *International Journal of Plasticity* 20.10 (Oct. 2004), pp. 1763–1788. ISSN: 0749-6419. DOI: 10.1016/j.ijplas.2003.11.014.

[12] X. F. Tang, L. F. Peng, S. Q. Shi, and M. W. Fu. "Influence of Crystal Structure on Size Dependent Deformation Behavior and Strain Heterogeneity in Micro-Scale Deformation". In: *International Journal of Plasticity* 118 (July 2019), pp. 147–172. ISSN: 0749-6419. DOI: 10.1016/j.ijplas.2019.02.004.

[13] Y. Hayashi, D. Setoyama, Y. Hirose, T. Yoshida, and H. Kimura. "Intragranular Three-Dimensional Stress Tensor Fields in Plastically Deformed Polycrystals". In: *Science* 366.6472 (Dec. 2019), pp. 1492–1496. ISSN: 0036-8075, 1095-9203. DOI: 10.1126/science.aax9167.

[14] E. C. Oliver, M. R. Daymond, and P. J. Withers. "Interphase and Intergranular Stress Generation in Carbon Steels". In: *Acta Materialia* 52.7 (Apr. 2004), pp. 1937–1951. ISSN: 1359-6454. DOI: 10.1016/j.actamat.2003.12.035.

[15] N. Allain-Bonasso, F. Wagner, S. Berbenni, and D. P. Field. "A Study of the Heterogeneity of Plastic Deformation in IF Steel by EBSD". In: *Materials Science and Engineering: A* 548 (June 2012), pp. 56–63. ISSN: 0921-5093. DOI: 10.1016/j.msea.2012.03.068.

[16] J. Marteau, H. Haddadi, and S. Bouvier. "Investigation of Strain Heterogeneities Between Grains in Ferritic and Ferritic-Martensitic Steels". In: *Experimental Mechanics* 53.3 (Mar. 2013), pp. 427–439. ISSN: 1741-2765. DOI: 10.1007/s11340-012-9657-6.

[17] J. Oddershede, J. P. Wright, A. Beaudoin, and G. Winther. "Deformation-Induced Orientation Spread in Individual Bulk Grains of an Interstitial-Free Steel". In: *Acta Materialia* 85 (Feb. 2015), pp. 301–313. ISSN: 1359-6454. DOI: 10.1016/j.actamat.2014.11.038.

[18] G. Winther, J. P. Wright, S. Schmidt, and J. Oddershede. "Grain Interaction Mechanisms Leading to Intragranular Orientation Spread in Tensile Deformed Bulk Grains of Interstitial-Free Steel". In: *International Journal of Plasticity* 88 (Jan. 2017), pp. 108–125. ISSN: 0749-6419. DOI: 10.1016/j.ijplas.2016.10.004.

[19] V. Khademi, T. R. Bieler, and C. J. Boehlert. "On the Correlation between Plastic Strain and Misorientation in Polycrystalline Body-Centered-Cubic Microstructures with an Emphasis on the Grain Size, Loading History, and Crystallographic Orientation". In: *International Journal of Plasticity* (Aug. 2021), p. 103084. ISSN: 0749-6419. DOI: 10.1016/j.ijplas.2021.103084.

[20] T. E. Buchheit, J. D. Carroll, B. G. Clark, and B. L. Boyce. "Evaluating Deformation-Induced Grain Orientation Change in a Polycrystal During In Situ Tensile Deformation Using EBSD". In: *Microscopy and Microanalysis* 21.4 (Aug. 2015), pp. 969–984. ISSN: 1431-9276, 1435-8115. DOI: 10.1017/S1431927615000677.

[21] J. D. Carroll, B. G. Clark, T. E. Buchheit, B. L. Boyce, and C. R. Weinberger. "An Experimental Statistical Analysis of Stress Projection Factors in BCC Tantalum". In: *Materials Science and Engineering: A* 581 (Oct. 2013), pp. 108–118. ISSN: 0921-5093. DOI: 10.1016/j.msea.2013.05.085.

[22] H. Lim, J. D. Carroll, C. C. Battaile, T. E. Buchheit, B. L. Boyce, and C. R. Weinberger. "Grain-Scale Experimental Validation of Crystal Plasticity Finite Element Simulations of Tantalum Oligocrystals". In: *International Journal of Plasticity* 60 (Sept. 2014), pp. 1–18. ISSN: 0749-6419. DOI: 10.1016/j.ijplas.2014.05.004.

[23] J. J. Bhattacharyya, S. Nair, D. C. Pagan, V. Tari, R. A. Lebensohn, A. D. Rollett, and S. R. Agnew. "Elastoplastic Transition in a Metastable $\beta$-Titanium Alloy, Timetal-18 – An in-Situ Synchrotron X-ray Diffraction Study". In: *International Journal of Plasticity* 139 (Apr. 2021), p. 102947. ISSN: 0749-6419. DOI: 10.1016/j.ijplas.2021.102947.

[24] J. J. Bhattacharyya, D. C. Pagan, and S. R. Agnew. "Large Rotations of the Grain-Scale Stress Tensor during Yielding Set the Stage for Failure". In: *International Journal of Plasticity* (Aug. 2021), p. 103087. ISSN: 0749-6419. DOI: 10.1016/j.ijplas.2021.103087.

[25] C. Efstathiou, D. E. Boyce, J. S. Park, U. Lienert, P. R. Dawson, and M. P. Miller. "A Method for Measuring Single-Crystal Elastic Moduli Using High-Energy X-ray Diffraction and a Crystal-Based Finite Element Model". In: *Acta Materialia* 58.17 (Oct. 2010), pp. 5806–5819. ISSN: 1359-6454. DOI: 10.1016/j.actamat.2010.06.056.

[26] R. Pokharel, J. Lind, S. F. Li, P. Kenesei, R. A. Lebensohn, R. M. Suter, and A. D. Rollett. "In-Situ Observation of Bulk 3D Grain Evolution during Plastic Deformation in Polycrystalline Cu". In: *International Journal of Plasticity* 67 (Apr. 2015), pp. 217–234. ISSN: 0749-6419. DOI: 10.1016/j.ijplas.2014.10.013.

[27] M. A. Charpagne, J. Hestroffer, A. T. Polonsky, M. P. Echlin, D. Texier, V. Valle, I. J. Beyerlein, T. M. Pollock, and J. C. Stinville. "Slip Localization in Inconel 718: A Three-Dimensional and Statistical Perspective". In: *Acta Materialia* (June 2021), p. 117037. ISSN: 1359-6454. DOI: 10.1016/j.actamat.2021.117037.

[28] F. Di Gioacchino and J. Q. da Fonseca. "An Experimental Study of the Polycrystalline Plasticity of Austenitic Stainless Steel". In: *International Journal of Plasticity* 74 (Nov. 2015), pp. 92–109. ISSN: 0749-6419. DOI: 10.1016/j.ijplas.2015.05.012.

[29] W. Q. Gao, C. L. Zhang, M. X. Yang, S. Q. Zhang, D. Juul Jensen, and A. Godfrey. "Strain Distribution and Lattice Rotations during In-Situ Tension of Aluminum with a Transmodal Grain Structure". In: *Materials Science and Engineering: A* (Sept. 2021), p. 142010. ISSN: 0921-5093. DOI: 10.1016/j.msea.2021.142010.

[30] A. Guery, F. Hild, F. Latourte, and S. Roux. "Slip Activities in Polycrystals Determined by Coupling DIC Measurements with Crystal Plasticity Calculations". In: *International Journal of Plasticity* 81 (June 2016), pp. 249–266. ISSN: 0749-6419. DOI: 10.1016/j.ijplas.2016.01.008.

[31] J. H. Liu, N. Vanderesse, J-C. Stinville, T. M. Pollock, P. Bocher, and D. Texier. "In-Plane and out-of-Plane Deformation at the Sub-Grain Scale in Polycrystalline Materials Assessed by Confocal Microscopy". In: *Acta Materialia* 169 (May 2019), pp. 260–274. ISSN: 1359-6454. DOI: 10.1016/j.actamat.2019.03.001.

[32] W. D. Musinski, P. A. Shade, D. C. Pagan, and J. V. Bernier. "Statistical Aspects of Grain-Level Strain Evolution and Reorientation during the Heating and Elastic-Plastic Loading of a Ni-base Superalloy at Elevated Temperature". In: *Materialia* (Mar. 2021), p. 101063. ISSN: 2589-1529. DOI: 10.1016/j.mtla.2021.101063.

[33] M. D. Sangid, J. Rotella, D. Naragani, J-S. Park, P. Kenesei, and P. A. Shade. "A Complete Grain-Level Assessment of the Stress-Strain Evolution and Associated Deformation Response in Polycrystalline Alloys". In: *Acta Materialia* 201 (Dec. 2020), pp. 36–54. ISSN: 1359-6454. DOI: 10.1016/j.actamat.2020.09.051.

[34] J. C. Stinville, N. Vanderesse, F. Bridier, P. Bocher, and T. M. Pollock. "High Resolution Mapping of Strain Localization near Twin Boundaries in a Nickel-Based Superalloy". In: *Acta Materialia* 98 (Oct. 2015), pp. 29–42. ISSN: 1359-6454. DOI: 10.1016/j.actamat.2015.07.016.

[35] M. A. Tschopp, B. B. Bartha, W. J. Porter, P. T. Murray, and S. B. Fairchild. "Microstructure-Dependent Local Strain Behavior in Polycrystals through In-Situ Scanning Electron Microscope Tensile Experiments". In: *Metallurgical and Materials Transactions A* 40.10 (Oct. 2009), pp. 2363–2368. ISSN: 1543-1940. DOI: 10.1007/s11661-009-9938-6.

[36] J. C. Stinville, M. A. Charpagne, F. Bourdin, P. G. Callahan, Z. Chen, M. P. Echlin, D. Texier, J. Cormier, P. Villechaise, T. M. Pollock, and V. Valle. "Measurement of Elastic and Rotation Fields during Irreversible Deformation Using Heaviside-digital Image Correlation". In: *Materials Characterization* 169 (Nov. 2020), p. 110600. ISSN: 1044-5803. DOI: 10.1016/j.matchar.2020.110600.

[37] J. W. Christian. "Some Surprising Features of the Plastic Deformation of Body-Centered Cubic Metals and Alloys". In: *Metallurgical Transactions A* 14.7 (July 1983), pp. 1237–1256. ISSN: 1543-1940. DOI: 10.1007/BF02664806.

[38] L. L. Hsiung. "On the Mechanism of Anomalous Slip in Bcc Metals". In: *Materials Science and Engineering: A*. Special Topic Section: Local and Near Surface Structure from Diffraction 528.1 (Nov. 2010), pp. 329–337. ISSN: 0921-5093. DOI: 10.1016/j.msea.2010.09.017.

[39] C. R. Weinberger, B. L. Boyce, and C. C. Battaile. "Slip Planes in Bcc Transition Metals". In: *International Materials Reviews* 58.5 (June 2013), pp. 296–314. ISSN: 0950-6608. DOI: 10.1179/1743280412Y.0000000015.

[40] B. Douat, C. Coupeau, J. Bonneville, M. Drouet, L. Vernisse, and L. Kubin. "Atomic-Scale Insight into Non-Crystallographic Slip Traces in Body-Centred Cubic Crystals". In: *Scripta Materialia* 162 (Mar. 2019), pp. 292–295. ISSN: 1359-6462. DOI: 10.1016/j.scriptamat.2018.10.032.

[41] M. Ben Haj Slama, N. Maloufi, J. Guyon, S. Bahi, L. Weiss, and A. Guitton. "In Situ Macroscopic Tensile Testing in SEM and Electron Channeling Contrast Imaging: Pencil Glide Evidenced in a Bulk $\beta$-Ti21S Polycrystal". In: *Materials* 12.15 (Jan. 2019), p. 2479. DOI: 10.3390/ma12152479.

[42] C. Du, F. Maresca, M. G. D. Geers, and J. P. M. Hoefnagels. "Ferrite Slip System Activation Investigated by Uniaxial Micro-Tensile Tests and Simulations". In: *Acta Materialia* 146 (Mar. 2018), pp. 314–327. ISSN: 1359-6454. DOI: 10.1016/j.actamat.2017.12.054.

[43] D. Caillard. "Kinetics of Dislocations in Pure Fe. Part I. In Situ Straining Experiments at Room Temperature". In: *Acta Materialia* 58.9 (May 2010), pp. 3493–3503. ISSN: 1359-6454. DOI: 10.1016/j.actamat.2010.02.023.

[44] P. Franciosi, L. T. Le, G. Monnet, C. Kahloun, and M. H. Chavanne. "Investigation of Slip System Activity in Iron at Room Temperature by SEM and AFM In-Situ Tensile and Compression Tests of Iron Single Crystals". In: *International Journal of Plasticity* 65 (Feb. 2015), pp. 226–249. ISSN: 0749-6419. DOI: 10.1016/j.ijplas.2014.09.008.

[45] V. Couty, J-F. Witz, C. Martel, F. Bari, and A. Weisrock. "CRAPPY: Command and Real-Time Acquisition in Parallelized Python, a Python Module for Experimental Setups". In: *SoftwareX* 16 (Dec. 2021), p. 100848. ISSN: 2352-7110. DOI: 10.1016/j.softx.2021.100848.

[46] G. Nicoletto, T. Marin, G. Anzelotti, and R. Roncella. "Application of High Magnification Digital Image Correlation Technique to Micromechanical Strain Analysis". In: *Strain* 47.s1 (2011), e66–e73. ISSN: 1475-1305. DOI: 10.1111/j.1475-1305.2008.00489.x.

[47] G. L. G. Gonzáles, J. A. O. González, J. T. Pinho de Castro, and J. L. de França Feire. "Measuring Elastoplastic Strain Loops in the near Crack-Tip Region Using a Stereo Microscope DIC System". In: *International Journal of Fatigue* 133 (Apr. 2020), p. 105427. ISSN: 0142-1123. DOI: 10.1016/j.ijfatigue.2019.105427.

[48] B. Pan. "Digital Image Correlation for Surface Deformation Measurement: Historical Developments, Recent Advances and Future Goals". In: *Measurement Science and Technology* 29.8 (June 2018), p. 082001. ISSN: 0957-0233. DOI: 10.1088/1361-6501/aac55b.

[49] N. Dahdah, N. Limodin, A. El Bartali, J. F. Witz, R. Seghir, E. Charkaluk, and J. Y. Buffiere. "Damage Investigation in A319 Aluminium Alloy by X-ray Tomography and Digital Volume Correlation during In Situ High-Temperature Fatigue Tests". In: *Strain* 52.4 (2016), pp. 324–335. ISSN: 1475-1305. DOI: 10.1111/str.12193.

[50] Z. Li, N. Limodin, A. Tandjaoui, P. Quaegebeur, J-F. Witz, and D. Balloy. "Influence of Fe Content on the Damage Mechanism in A319 Aluminum Alloy: Tensile Tests and Digital Image Correlation". In: *Engineering Fracture Mechanics*. Modern Imaging Techniques in Fracture and Damage Analyses 183 (Oct. 2017), pp. 94–108. ISSN: 0013-7944. DOI: 10.1016/j.engfracmech.2017.05.006.

[51] B. Winiarski, A. Gholinia, K. Mingard, M. Gee, G. Thompson, and P. J. Withers. "Correction of Artefacts Associated with Large Area EBSD". In: *Ultramicroscopy* 226 (July 2021), p. 113315. ISSN: 0304-3991. DOI: 10.1016/j.ultramic.2021.113315.

[52] F. L. Bookstein. "Principal Warps: Thin-Plate Splines and the Decomposition of Deformations". In: *IEEE Transactions on Pattern Analysis and Machine Intelligence* 11.6 (June 1989), pp. 567–585. ISSN: 1939-3539. DOI: 10.1109/34.24792.

[53] P. Baudoin. "Caractérisation et Identification de Propriétés de Matériaux Métalliques à Gradients de Microstructure". Mécanique. Lille 1, Apr. 2015.

[54] J. K. Mackenzie and M. J. Thomson. "Some Statistics Associated with the Random Disorientation of Cubes". In: *Biometrika* 44.1-2 (June 1957), pp. 205–210. ISSN: 0006-3444. DOI: 10.1093/biomet/44.1-2.205.

[55] M. Ben Haj Slama, V. Taupin, N. Maloufi, K. Venkatraman, A. D. Rollett, R. A. Lebensohn, S. Berbenni, B. Beausir, and A. Guitton. "Electron Channeling Contrast Imaging Characterization and Crystal Plasticity Modelling of Dislocation Activity in Ti21S BCC Material". In: *Materialia* 15 (Mar. 2021), p. 100996. ISSN: 2589-1529. DOI: 10.1016/j.mtla.2020.100996.

[56] H. Zhang, J. Liu, D. Sui, Z. Cui, and M. W. Fu. "Study of Microstructural Grain and Geometric Size Effects on Plastic Heterogeneities at Grain-Level by Using Crystal Plasticity Modeling with High-Fidelity Representative Microstructures". In: *International Journal of Plasticity* 100 (Jan. 2018), pp. 69–89. ISSN: 0749-6419. DOI: 10.1016/j.ijplas.2017.09.011.

[57] M. R. Stoudt, L. E. Levine, A. Creuziger, and J. B. Hubbard. "The Fundamental Relationships between Grain Orientation, Deformation-Induced Surface Roughness and Strain Localization in an Aluminum Alloy". In: *Materials Science and Engineering: A* 530 (Dec. 2011), pp. 107–116. ISSN: 0921-5093. DOI: 10.1016/j.msea.2011.09.050.

[58] X. Hong, A. Godfrey, C. L. Zhang, W. Liu, and A. Chapuis. "Investigation of Grain Subdivision at Very Low Plastic Strains in a Magnesium Alloy". In: *Materials Science and Engineering: A* 693 (May 2017), pp. 14–21. ISSN: 0921-5093. DOI: 10.1016/j.msea.2017.03.080.

[59] A. Kundu and D. P. Field. "Geometrically Necessary Dislocation Density Evolution in Interstitial Free Steel at Small Plastic Strains". In: *Metallurgical and Materials Transactions A* 49.8 (Aug. 2018), pp. 3274–3282. ISSN: 1543-1940. DOI: 10.1007/s11661-018-4693-1.

[60] S. I. Wright, S. Suzuki, and M. M. Nowell. "In Situ EBSD Observations of the Evolution in Crystallographic Orientation with Deformation". In: *JOM* 68.11 (Nov. 2016), pp. 2730–2736. ISSN: 1543-1851. DOI: 10.1007/s11837-016-2084-x.

[61] J. H. Zar. "Spearman Rank Correlation". In: *Encyclopedia of Biostatistics*. American Cancer Society, 2005. ISBN: 978-0-470-01181-2. DOI: 10.1002/0470011815.b2a15150.

[62] Z. Zhang, D. Lunt, H. Abdolvand, A. J. Wilkinson, M. Preuss, and F. P. E. Dunne. "Quantitative Investigation of Micro Slip and Localization in Polycrystalline Materials under Uniaxial Tension". In: *International Journal of Plasticity* 108 (Sept. 2018), pp. 88–106. ISSN: 0749-6419. DOI: 10.1016/j.ijplas.2018.04.014.

[63] S. L. Wong and P. R. Dawson. "Influence of Directional Strength-to-Stiffness on the Elastic–Plastic Transition of Fcc Polycrystals under Uniaxial Tensile Loading". In: *Acta Materialia* 58.5 (Mar. 2010), pp. 1658–1678. ISSN: 1359-6454. DOI: 10.1016/j.actamat.2009.11.009.

[64] S. J. Vachhani, R. D. Doherty, and S. R. Kalidindi. "Studies of Grain Boundary Regions in Deformed Polycrystalline Aluminum Using Spherical Nanoindentation". In: *International Journal of Plasticity* 81 (June 2016), pp. 87–101. ISSN: 0749-6419. DOI: 10.1016/j.ijplas.2016.01.001.

[65] A. Zeghadi, F. N'guyen, S. Forest, A.-F. Gourgues, and O. Bouaziz. "Ensemble Averaging Stress–Strain Fields in Polycrystalline Aggregates with a Constrained Surface Microstructure – Part 1: Anisotropic Elastic Behaviour". In: *Philosophical Magazine* 87.8-9 (Mar. 2007), pp. 1401–1424. ISSN: 1478-6435. DOI: 10.1080/14786430601009509.

[66] A. Zeghadi, S. Forest, A.-F. Gourgues, and O. Bouaziz. "Ensemble Averaging Stress–Strain Fields in Polycrystalline Aggregates with a Constrained Surface Microstructure – Part 2: Crystal Plasticity". In: *Philosophical Magazine* 87.8-9 (Mar. 2007), pp. 1425–1446. ISSN: 1478-6435. DOI: 10.1080/14786430601009517.

[67] Z. Chen and S. H. Daly. "Active Slip System Identification in Polycrystalline Metals by Digital Image Correlation (DIC)". In: *Experimental Mechanics* 57.1 (Jan. 2017), pp. 115–127. ISSN: 1741-2765. DOI: 10.1007/s11340-016-0217-3.

[68] W. Abuzaid, M. D. Sangid, J. D. Carroll, H. Sehitoglu, and J. Lambros. "Slip Transfer and Plastic Strain Accumulation across Grain Boundaries in Hastelloy X". In: *Journal of the Mechanics and Physics of Solids* 60.6 (June 2012), pp. 1201–1220. ISSN: 0022-5096. DOI: 10.1016/j.jmps.2012.02.001.

[69] F. Di Gioacchino, T. E. J. Edwards, G. N. Wells, and W. J. Clegg. "A New Mechanism of Strain Transfer in Polycrystals". In: *Scientific Reports* 10.1 (June 2020), p. 10082. ISSN: 2045-2322. DOI: 10.1038/s41598-020-66569-7.

[70] S. Papanikolaou, Y. Cui, and N. Ghoniem. "Avalanches and Plastic Flow in Crystal Plasticity: An Overview". In: *Modelling and Simulation in Materials Science and Engineering* 26.1 (Dec. 2017), p. 013001. ISSN: 0965-0393. DOI: 10.1088/1361-651X/aa97ad.

[71] E. Bayerschen, A. T. McBride, B. D. Reddy, and T. Böhlke. "Review on Slip Transmission Criteria in Experiments and Crystal Plasticity Models". In: *Journal of Materials Science* 51.5 (Mar. 2016), pp. 2243–2258. ISSN: 1573-4803. DOI: 10.1007/s10853-015-9553-4.

[72] F. Shuang and K. E. Aifantis. "Using Molecular Dynamics to Determine Mechanical Grain Boundary Energies and Capture Their Dependence on Residual Burgers Vector, Segregation and Grain Size". In: *Acta Materialia* 195 (Aug. 2020), pp. 358–370. ISSN: 1359-6454. DOI: 10.1016/j.actamat.2020.05.014.

[73] L. Patriarca, W. Abuzaid, H. Sehitoglu, and H. J. Maier. "Slip Transmission in Bcc FeCr Polycrystal". In: *Materials Science and Engineering: A* 588 (Dec. 2013), pp. 308–317. ISSN: 0921-5093. DOI: 10.1016/j.msea.2013.08.050.

[74] Z. Csati, J-F. Witz, V. Magnier, A. El Bartali, N. Limodin, and D. Najjar. "CristalX: Facilitating Simulations for Experimentally Obtained Grain-Based Microstructures". In: *SoftwareX* 14 (June 2021), p. 100669. ISSN: 2352-7110. DOI: 10.1016/j.softx.2021.100669.

[75] F. Bridier, P. Villechaise, and J. Mendez. "Analysis of the Different Slip Systems Activated by Tension in a Alpha/Beta Titanium Alloy in Relation with Local Crystallographic Orientation". In: *Acta Materialia* 53.3 (Feb. 2005), pp. 555–567. ISSN: 1359-6454. DOI: 10.1016/j.actamat.2004.09.040.

[76] T. H. Courtney. *Mechanical Behavior of Materials: Second Edition*. Waveland Press, Dec. 2005. ISBN: 978-1-4786-0838-7.

[77] A. E. Lord and D. N. Beshers. "Elastic Stiffness Coefficients of Iron from 77 to 673K". In: *Journal of Applied Physics* 36.5 (May 1965), pp. 1620–1623. ISSN: 0021-8979. DOI: 10.1063/1.1703098.